

Abstract

Astronomers have learnt a lot about the formation and evolution of structure in the universe by studying the Lyman Alpha forest, or clouds of atomic hydrogen distributed throughout the universe. Since atomic hydrogen cannot exist at high temperatures, this gas is not very luminous, so needs to be observed by other means, such as the absorption lines it produces in the spectra of background quasars. In this report, I present simulations showing how the small scale structure of the Lyman Alpha clouds could be measured by observing the spectra of a gravitationally lensed quasar over a period of time. The strength of the Lyman Alpha absorption lines relative to the continuum in the spectrum of a microlensed quasar is shown to vary with time, with the properties of the variations depending on the structure of the absorbing material. I conclude that such variations will be measurable via UV spectroscopy of image A of the lensed quasar Q2237+0305 if the Lyman Alpha clouds between the quasar and the lensing galaxy possess structure on scales smaller than ~ 0.1 pc. The time-scale for variations is on the order of decades, although very short term variability can occur.

Acknowledgements

Firstly, I would like to thank my supervisor, Dr Geraint F. Lewis, for suggesting such a great topic to work on, for always convincing me that something was worth trying even when I thought it was useless (regarding Figure 4.7, I stand by my opinions), and for always producing a *faultergeist*¹ whenever something went wrong.

I would like to thank Mathworks, for producing the excellent (in my opinion) program MATLAB which I used for much of the project, particularly to produce most of the graphics.

I would like to thank my parrot Zazu, for all the kind support she has provided me as I stressed (quite unnecessarily) about the completion of this thesis. I would like to thank the SSSF (<http://www2b.abc.net.au/science/k2/stn/>), for what I am not sure, but I will anyway. I would like to thank my family, particularly my Nanna, for doing too much for me at home so that I can bludge so much during the year and still hopefully do well at uni.

Finally, I would like to thank the following bands/musicians for entertaining me during the year: Split Enz, Tim Finn, Duran Duran, Pat Metheny Group, Radiohead and Steely Dan.

The results from this honours project have been accepted for publication in the Monthly Notices of the Royal Astronomical Society (Brewer & Lewis, 2004). A copy of this publication is included at the end of this report.

Statement of Contribution of the Student

The idea for this study came from my supervisor, Dr Geraint Lewis. The FORTRAN code which was the basis of most of what I did was originally written by Joachim Wambsganss and modified by Geraint Lewis. Most of the methods and models described in Chapters 1 and 2 were originally created by others, but the methods used for including absorption (Chapter 3) and basically everything after that is my original research. Several figures in this report (mostly in the introduction), are taken from other sources, but have been acknowledged.

*I certify that this report contains work carried out
by myself except where otherwise acknowledged.*

Signed

Date: 22 October, 2004 C.E.

¹This is what occurs when something goes wrong, and seeking help from somebody magically fixes the problem, before they have actually done anything.

Contents

1	Introduction	1
1.1	Quasars	1
1.2	The Lyman Alpha Forest	1
1.3	Gravitational Lensing	4
1.3.1	Aside: Angular Diameter Distances	5
1.3.2	Back to Gravitational Lensing	5
1.3.3	Microlensing	7
1.4	Magnification Maps	8
2	Microlensing	11
2.1	Backwards Ray-Shooting Method	11
2.2	External Shear	13
2.3	Model Parameters	13
2.4	Extended Sources	14
3	Including Cosmological Absorption	15
3.1	Absorption Clouds	15
3.2	Distances and Cosmology	16
3.3	Line Strength Maps	19
4	Results	20
4.1	Line Strength Maps	20
4.2	Time Scales	27
4.3	Caustic Crossings	31
5	Conclusion	33
5.1	Further Work, Observational Prospects	33

Chapter 1

Introduction

Cosmology is the study of the history and evolution of the universe. Observational cosmology is difficult area of astronomy, as in order to learn much about the history of the universe, observations of the some of the most distant objects in the universe are required - these objects are ones that emitted their light when the universe was much younger.

However, not every object of interest in the universe is luminous enough to be detected by telescopes. Indeed, some components of the universe, such as dark matter, are thought not to emit any electromagnetic radiation at all. This is unfortunate, considering that dark matter is the dominant factor driving the formation of structure in the universe, with other components such as gas and galaxies essentially being taken along for the ride. Galaxies are relatively luminous, and can be observed at low redshifts, as can hot intergalactic gas as it emits at the x-ray and UV wavelengths. However, cooler gas such as atomic or molecular hydrogen is very hard to observe directly.

In order to observe these less luminous objects in the universe, novel (often indirect) methods are required. In this project, I investigated one new method for looking at the small-scale structure of distant intergalactic gas (which could be related to star formation in the the distant past), using the phenomenon of gravitational microlensing.

1.1 Quasars

Quasars, or Quasi-Stellar Objects (QSOs) are among the most luminous objects observed in the universe. In fact, they are thought to be the brightest non-transient objects in the universe, with their emission powered by material falling onto the central black hole of a galaxy, producing a luminosity of about 100 times that of the host galaxy (Broderick, 2004). Since they are mostly observed at very large distances, they are faint when observed from Earth, and are highly redshifted due to the expanding universe (quasars are observed at many redshifts, though most are observed with redshifts in the range $z \simeq 1$ to about $z \simeq 5$). Due to their immense distance, they appear point-like when viewed in the optical region of the electromagnetic spectrum (Schmidt, 1963). Their high luminosity and the fact that quasars can be found at high redshifts are the main reasons why quasars are often used as cosmological probes (Marziani et al., 2003).

1.2 The Lyman Alpha Forest

The Lyman Alpha (Ly_α) forest is an absorption phenomenon which is observed in the spectra of many high redshift quasars. It arises due to absorption by galactic and intergalactic neutral hydrogen between a quasar and

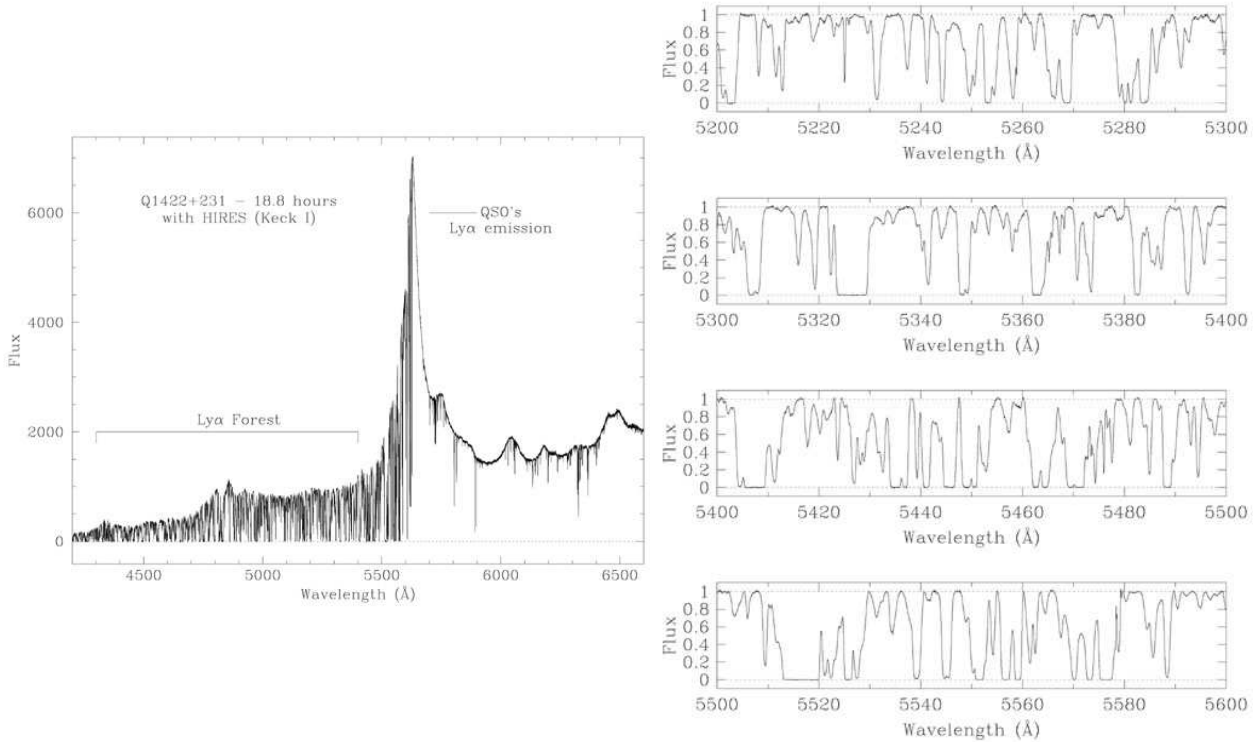


Figure 1.1: A portion of the spectrum of the gravitationally lensed quasar Q1422+231 (at a redshift of $z = 3.628$), showing the Lyman Alpha forest absorption lines on the blue (left) side of the quasar’s Ly $_{\alpha}$ emission line (Ellison, 2000). Other absorption lines due to metals in the Lyman Alpha Forest can be seen on the other side of the prominent Ly $_{\alpha}$ emission line. The plot on the right shows the Lyman Alpha forest lines at higher resolution. Each line corresponds to a distinct absorption “cloud” at a particular redshift.

an observer (see Rauch (1998) for a recent review). Due to the expansion of the universe, the quasar’s spectrum is gradually redshifted as it travels away from the quasar. When it encounters a cloud of neutral hydrogen, an absorption line is formed in the spectrum at a wavelength of 121.6 nm. The resulting spectrum observed at Earth contains many absorption lines blueward of the Ly $_{\alpha}$ emission line of the quasar, and the structure of the absorbing material along the line of sight is imprinted on the spectrum (e.g. Lu et al., 1996). See refspecc for an example of a high resolution quasar spectrum (Q1422+231) showing the Ly $_{\alpha}$ forest absorption lines. The absorption lines close to the Ly $_{\alpha}$ emission line of the quasar are due to gas closer to the quasar.

Numerical simulations of large-scale structure formation in the universe, have been largely based around the gravitational dynamics of dark matter, since it is the dominant mass component (Spergel et al., 2003). However, recently it has been possible to include gas, with its more complicated physics (including cooling, shocking and star formation) in the cosmological simulations, in order to predict the large scale structure of the gas (Davé et al., 1999, see Figure 1.2). The results of such simulations can then be compared with observations of the absorption lines in quasar spectra. The conclusions of these studies are that the Ly $_{\alpha}$ “clouds” are mostly intergalactic structures, with the denser regions corresponding to the locations where galaxies and galaxy clusters form. The outcomes of the simulations depend on the specified values of the cosmological parameters and the nature of the dark matter in the universe, so measurements of the structural properties of the Ly $_{\alpha}$ forest can be used to distinguish different cosmologies (e.g. McDonald & Miralda-Escudé, 1999).

Traditionally, the large scale structure of the Ly $_{\alpha}$ Forest has been the main focus of research, because of its cosmological significance (e.g. McDonald & Miralda-Escudé, 1999). The absorbing gas along the line of sight

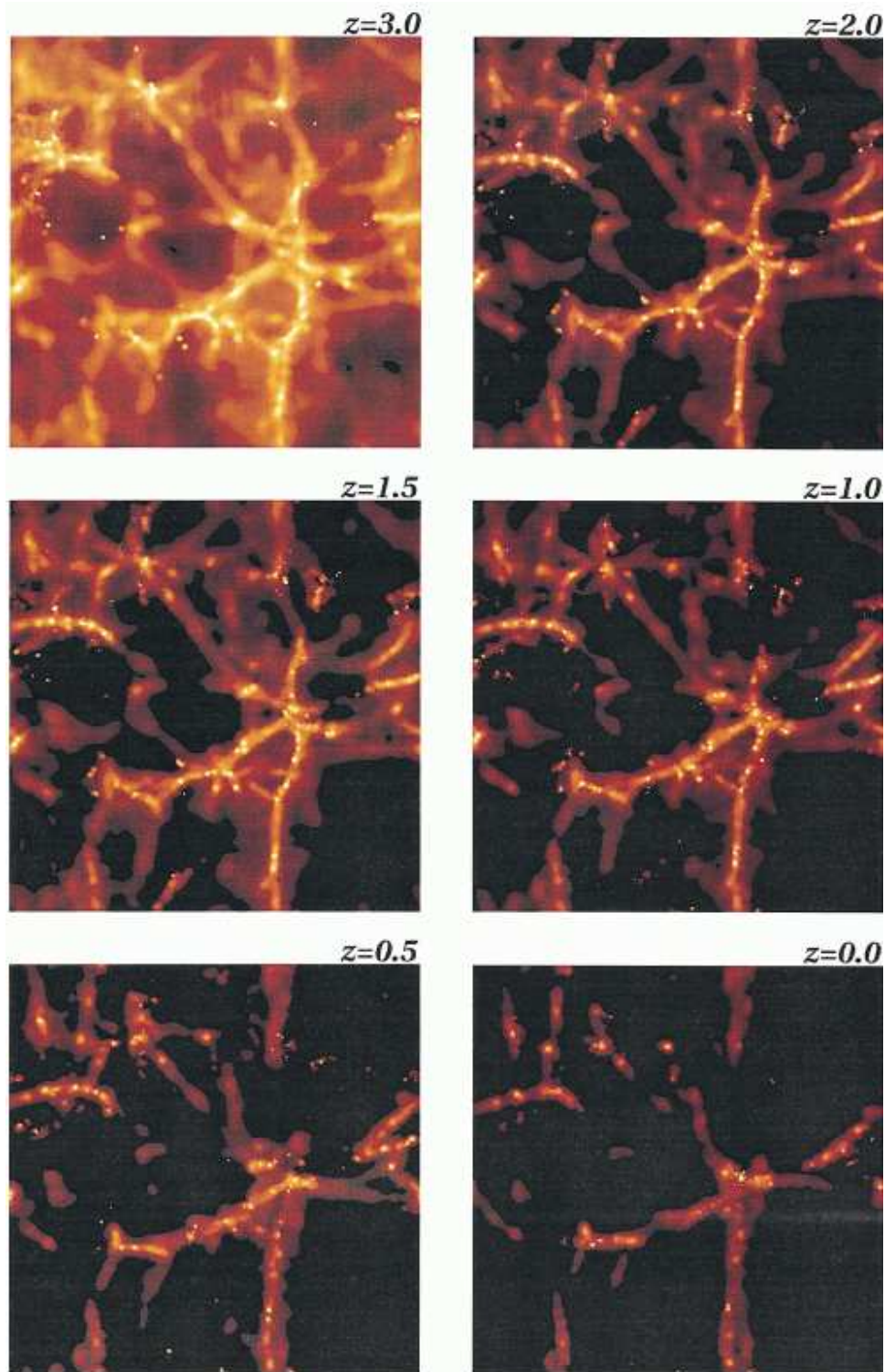


Figure 1.2: Simulations of the formation of the Lyman Alpha forest, from Davé et al. (1999). The images show the structure of the neutral hydrogen distribution across the sky at different redshifts z , corresponding to different times in the universe's history when the universe was $1/(1+z)$ times its current size. The evolution of the large scale structure is driven by the collapse and clustering of dark matter, since this is the dominant mass component. Gas too, collapses with the dark matter, causing the distribution to become less uniform with time (starting from the top plots, moving down), with the gas concentrated into the filamentary structures that can be seen.

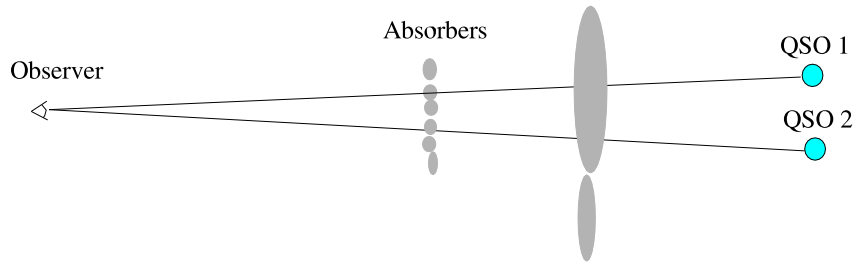


Figure 1.3: Diagram showing a pair of quasars on the sky and the effect of different cloud sizes. For the large clouds, the Lyman alpha forest lines in the spectra of the two quasars would be correlated, whereas for the small clouds they would be independent.

to a single quasar can be probed by comparing the relative positions and strengths of the absorption lines in the Ly_α forest in the spectrum of the quasar (Sargent et al., 1980). The structure across the line of sight is harder to measure, although two quasars that are nearby on the sky can be observed; the fraction of Ly_α forest lines that are common to the two quasars providing a measure of the extent of the clouds across the sky (Sargent, Young, & Schneider, 1982; Rollinde et al., 2003). The higher the degree of correlation between the absorption lines in the two spectra, the larger the typical structures are in the neutral hydrogen gas. Figure 1.3 illustrates this idea.

Recently, the small scale structure (on kiloparsec scales) has also been investigated by several methods (Rauch, Sargent, & Barlow, 1999, 2001; Rauch et al., 2001, 2002); potentially revealing structure in and about the interstellar medium in young galaxies. However, the very small scale (less than a parsec) structure of the Ly_α clouds is completely unknown (due to limits in observational techniques, and the fact that the resolution of Ly_α forest formation simulations is too coarse), and would be useful for deciding what the local equivalents of the Ly_α clouds are; for example, do the Lyman Alpha clouds resemble star forming regions with gas clumped on various scales, or is the gas still smoothly distributed? Some (but not all) low redshift Ly_α clouds have been found to be associated with galaxies (Salpeter & Hoffman, 1995), suggesting that the structure of the Ly_α clouds might mimic that of the interstellar medium, exhibiting fractal structure (Elmegreen, 1997). In this report, simulations are presented that demonstrate how the very small, sub parsec scales of Ly_α clouds (or any other absorption system) could be measured using a quasar that is subject to gravitational microlensing by a foreground galaxy.

1.3 Gravitational Lensing

In addition to quasar pairs (Figure 1.3), gravitational lensing provides a way to obtain multiple lines of sight through Lyman Alpha clouds. Gravitational lensing arises from one of the most important predictions of Einstein's theory of general relativity, that the paths of light rays are deflected as the light passes near a massive object. This implies that if a distant point source is observed, and a massive object lies between the source and the observer, the apparent position of the source is changed [see (Wambsganss, 1998) for a review of gravitational lensing]. Since this is analogous to the bending of light when an object is viewed through a glass lens, the phenomenon is called gravitational lensing. A diagram illustrating this idea is shown in Figure 1.4. The distances D_{ol} , D_{os} and D_{ls} are the angular diameter distances (see next subsection) from the observer to the lens, the observer to the source, and the lens to the source. Note that, in general, $D_{os} \neq D_{ol} + D_{ls}$.

1.3.1 Aside: Angular Diameter Distances

In Euclidean geometry, if an object has a physical length L and is placed at a distance D from an observer, the angular size θ of the object is given by

$$\theta = 2\tan^{-1}\left(\frac{L}{2D}\right) \approx \frac{L}{D} \quad (1.1)$$

where the approximation applies if the distance to the object is large compared to its length ($D \gg L$).

In non-Euclidean geometry, which can arise in general relativity (and hence cosmology), the simple inverse relationship between proper distance and angular diameter does not apply. Instead, to calculate the angular diameter of an object, the paths of two light rays in spacetime (one originating from each end of the object) have to be calculated, and their directions of arrival at the observer compared. Typically, a new type of “distance” is defined, called the *angular diameter distance* D_θ , such that the inverse relationship holds in terms of the angular diameter distance:

$$\theta = \frac{L}{D_\theta} \quad (1.2)$$

In cosmology, the spacetime is described by a Friedmann-Robertson-Walker metric. For a flat universe, this is

$$ds^2 = c^2 dt^2 - R(t)^2 [dr^2 + r^2 d\theta^2 + r^2 \sin^2 \theta d\phi^2] \quad (1.3)$$

From this metric, a differential equation can be derived which gives angular diameter distance as a function of redshift (Kayser, Helbig, & Schramm, 1997). Throughout the project, the assumed cosmology was a flat Big Bang cosmology with normalised matter density $\Omega_m = 0.3$, cosmological constant $\Omega_\Lambda = 0.7$ and Hubble’s constant $H_0 = 72 \text{ km s}^{-1} \text{ Mpc}^{-1}$. These are close to the values in the now dominant cosmological model (Spergel et al., 2003). Whenever it was required to convert a redshift to an angular diameter distance in this project, the program provided by Kayser, Helbig, & Schramm (1997) was used.

1.3.2 Back to Gravitational Lensing

If a light source is positioned at a point $\mathbf{R}_s \equiv (X_s, Y_s)$ in the *source plane* and a light ray from this source is observed, it will appear to have arrived from a different place, due to the deflection of the ray by the gravitational lens. The apparent position of the light source is given by a position $\mathbf{R} \equiv (X, Y)$ in the *image plane* or *lens plane*. Using simple geometry applied to Figure 1.4, it can be shown that the relationship between \mathbf{R} and \mathbf{R}_s is given by

$$\mathbf{R}_s = \frac{D_{os}}{D_{ol}} \mathbf{R} - D_{ls} \mathbf{A}(\mathbf{R}) \quad (1.4)$$

where D_{os} , D_{ol} and D_{ls} are the angular diameter distances from the observer to the source, observer to the lens, and lens to source respectively. The deflection angle $\mathbf{A}(\mathbf{R})$ is a vector function defined over the lens plane, and its form depends on how the mass in the gravitational lens is distributed over the source plane. Note that equation 1.4 gives a unique source plane position \mathbf{R}_s for a given image plane position \mathbf{R} . In general, though, the inverse function does not exist, so any particular position \mathbf{R}_s in the source plane can be mapped to multiple positions in the lens plane. This is the mathematical reason why the background source is often multiply imaged in gravitational lens systems. An example of a gravitationally lensed quasar with multiple images is the quasar Q2237+0305 (Huchra et al., 1985), an image of which is shown in Figure 1.5. The background

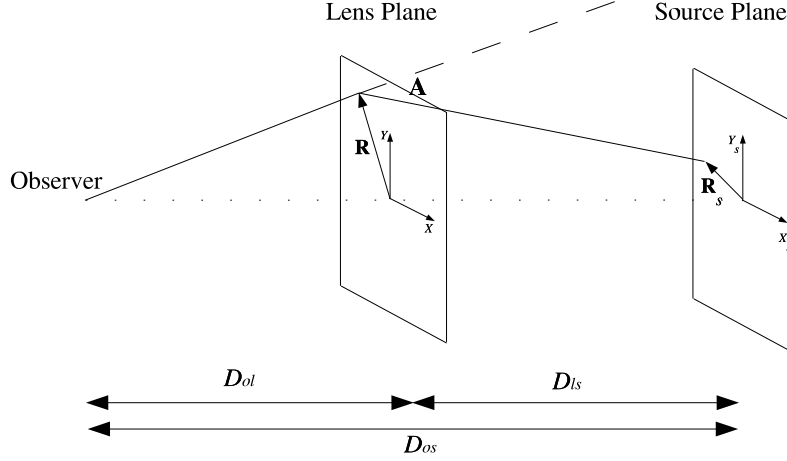


Figure 1.4: The geometrical setup used for modelling gravitational lensing (Schneider, Ehlers, & Falco, 1992). The lensing object is assumed to have its mass distributed in a plane, and the light rays undergo a sharp deflection at the lens plane. The lens plane is also where the image is formed.

quasar at a redshift of 1.695 has been gravitationally lensed by a foreground spiral galaxy at a redshift of 0.0394, producing four images of the quasar, positioned around the centre of the galaxy. Q2237+0305 is often nicknamed the “Einstein Cross” due to its appearance.

It can be shown from the general theory of relativity that the deflection angle $\mathbf{A}(\mathbf{R})$ for a point mass lens at the origin of the lens plane is given by

$$\mathbf{A}(\mathbf{R}) = -\frac{4GM}{c^2|\mathbf{R}|}\hat{\mathbf{R}} \quad (1.5)$$

where G is Newton’s gravitational constant, c is the speed of light in vacuum and M is the mass of the point gravitational lens. Interestingly, a similar result can be derived from either special relativity or Newtonian mechanics [assuming a $1/r^2$ gravitational field and that light is particles that travel at c , see Schneider, Ehlers, & Falco (1992)], although it is a factor of 2 smaller.

The result for a point mass lens is generalised to arbitrary continuous mass distributions $\rho(\mathbf{R})$ by integrating the deflection angle due to each small mass element of the gravitational lens, using 1.5 as the Green’s function:

$$\mathbf{A}(\mathbf{R}) = \frac{4GM}{c^2} \iint_L \frac{\mathbf{R} - \mathbf{R}'}{|\mathbf{R} - \mathbf{R}'|^2} \rho(\mathbf{R}') d^2\mathbf{R}' \quad (1.6)$$

If the lens is composed of N discrete point masses at positions \mathbf{R}_i with masses M_i , the integral is replaced by a sum:

$$\mathbf{A}(\mathbf{R}) = \frac{4GM}{c^2} \sum_{i=1}^N \frac{\mathbf{R} - \mathbf{R}_i}{|\mathbf{R} - \mathbf{R}_i|^2} M_i \quad (1.7)$$

For a point mass lens located at $\mathbf{R} = (0, 0)$ and a point source at the origin of the source plane, $[\mathbf{R}_s = (0, 0)]$, the observed image would be a circular ring with an angular radius approximately equal to the *angular Einstein Radius*

$$\theta_0 = \sqrt{\frac{4GM}{c^2} \frac{D_{ls}}{D_{ol}D_{os}}} \quad (1.8)$$

This is because any point in the lens plane at a distance $D_{ol}\theta_0$ (an Einstein Radius in the lens plane) from the origin is mapped via 1.4 onto the origin of the source plane. The Einstein Radius provides a convenient length scale for discussing gravitational lensing. Typically, the coordinates \mathbf{R} and \mathbf{R}_s are replaced by the scaled coordinates

$$\mathbf{r} \equiv \frac{\mathbf{R}}{D_{ol}\theta_0} \quad (1.9)$$

$$\mathbf{r}_s \equiv \frac{\mathbf{R}_s}{D_{os}\theta_0} \quad (1.10)$$

The scaled deflection angle \mathbf{a} is introduced:

$$\mathbf{a} = \frac{D_{ls}}{D_{os}\theta_0} \mathbf{A} \quad (1.11)$$

With these changes, the lensing equation 1.4 takes following simple form, referred to as the *normalised lens equation*:

$$\mathbf{r}_s = \mathbf{r} - \mathbf{a}(\mathbf{r}) \quad (1.12)$$

In addition, the surface mass density $\rho(\mathbf{R})$ is replaced by the dimensionless surface mass density

$$\sigma = \frac{4\pi G}{c^2} \frac{D_{ol}D_{ls}}{D_{os}} \rho \quad (1.13)$$

This change eliminates the prefactors from the scaled versions of Equations 1.6 and 1.7.

Gravitational lensing has previously been used to probe the size of Ly_α absorbing clouds. When the background quasar (regarded as a point source) is lensed by a foreground galaxy, multiple images of the quasar may be obtained. The light rays responsible for the two different images have traversed slightly different regions of space in their journey to the observer. Hence, a measure of the size of the Ly_α absorbing clouds (down to kiloparsec scales) can be made by cross-correlating the the absorption lines in two images of the same quasar (Ellison et al., 2004; Becker, Sargent, & Rauch, 2003). This method is analogous to the above method which uses a pair of quasars, however the lensing supplies a “pair” of quasars that are very close together on the sky, allowing smaller scale structure to be studied than is possible with the pairs of quasars on the sky. Rauch, Sargent, & Barlow (1999) used this method in the multiply imaged quasar Q1422+231 to trace MgII and CIV absorption clouds between the lens and the quasar down to scales of ~ 26 pc, which is the smallest scale so far considered. On the larger scales, McGill (1990) showed (using quasar pairs) that the Lyman Alpha forest contains coherent structures with sizes $\sim 3 - 300$ kpc.

1.3.3 Microlensing

When gravitational lensing models are developed to explain the multiple images observed, the lensing galaxy is usually modelled by a smooth mass distribution $\rho(\mathbf{R})$ (e.g. Schneider et al., 1988). However, lensing galaxies aren't really a smooth mass distribution, but is also composed of compact objects such as stars, planets and

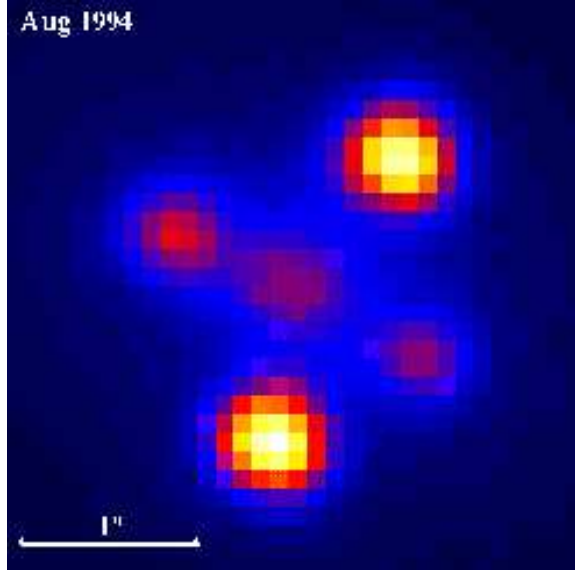


Figure 1.5: The gravitationally lensed quasar Q2237+0305 (Lewis et al., 1998). There are four images of the quasar, the central signal is residual light from the foreground lensing galaxy. The fact that the images are not points is due to seeing (atmospheric distortions and optical limitations).

black holes. Thus, the deflection angle for a ray passing through the lensing galaxy is not exactly as given by the smooth “macrolensing” model. This does not significantly affect the configuration of the images as observed on the sky. However, if an infinitely powerful telescope was available, each image of the quasar would be seen to be composed of many smaller *micro-images* (see Figure 1.6). This is the essential difference between a genuine smooth matter gravitational lens and one which is smooth on large scales but is made up of discrete point masses on small scales.

These micro-images cannot be observed directly, since they are so small, with typical angular separations of 1-2 micro arcseconds (Wambsganss, 1998). However, an observable effect occurs due to the motion of the galaxy across the line of sight to the quasar. As the foreground galaxy drifts across the line of sight to the quasar, the cluster of micro-images which forms a macro-image of the quasar can change its form, since the point lenses are now in different positions in the lens plane. Particularly, the total area of the micro-images can change significantly with time. Since surface brightness is constant along a particular ray, this implies that the brightness of the macro-image will change with time.

1.4 Magnification Maps

For a point source, the brightness of a macro-image is determined by the number of unresolvable micro-images it is composed of. For an extended source, the equivalent quantity is given by the integrated surface brightness over the image plane. If the surface brightness distribution of an image at time t is described by a function $b(\mathbf{r}, t)$ over the lens plane, then the observed total brightness is

$$\text{brightness}(t) \propto \iint_L b(\mathbf{r}, t) d^2\mathbf{r} = \iint_S s(\mathbf{r}_s, t) \mu(\mathbf{r}_s) d^2\mathbf{r}_s \quad (1.14)$$

where $s(\mathbf{r}_s, t)$ is the source profile at time t and μ is the reciprocal of the Jacobian determinant (Weisstein, 1999) of the lens mapping 1.12.

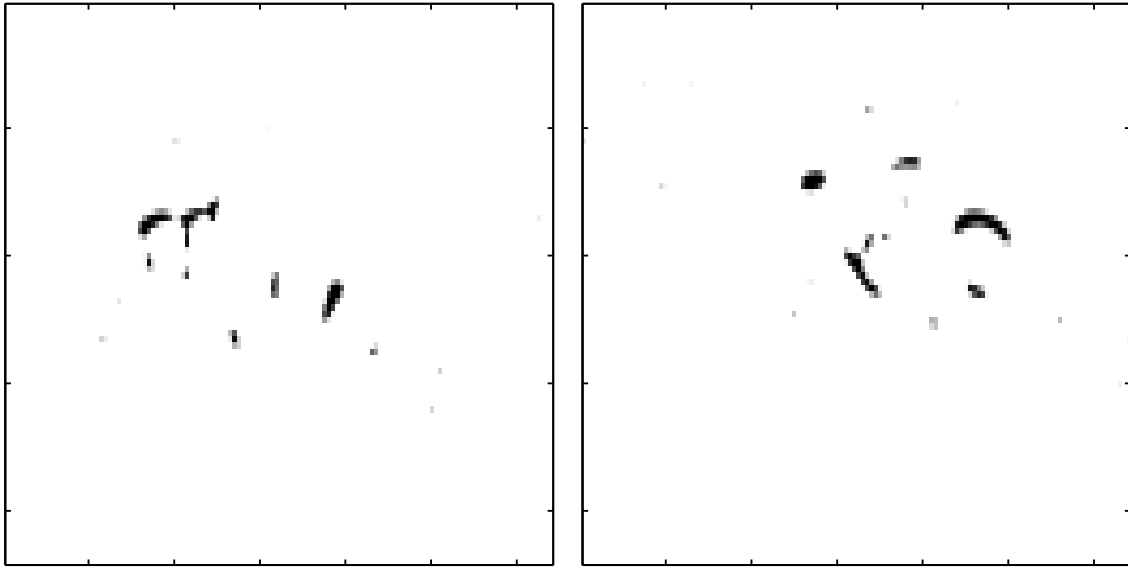


Figure 1.6: Simulations of the view of a single circular source through a field of microlensing point masses. In principle, any macro-image of a lensed quasar is actually composed of a myriad of micro-images like these. They cannot be resolved with telescopes as they are on microarcsecond scales, but the area of them (and hence the overall brightness of the image) changes with time as the quasar moves across the line of sight, relative to the stars in the lensing galaxy. The two pictures show the micro-images at different times, which are different due to the motion of the stars in the lensing galaxy relative to the background source. If the integrated brightness of the micro-images has changed, then the observed brightness of the image will be seen to change.

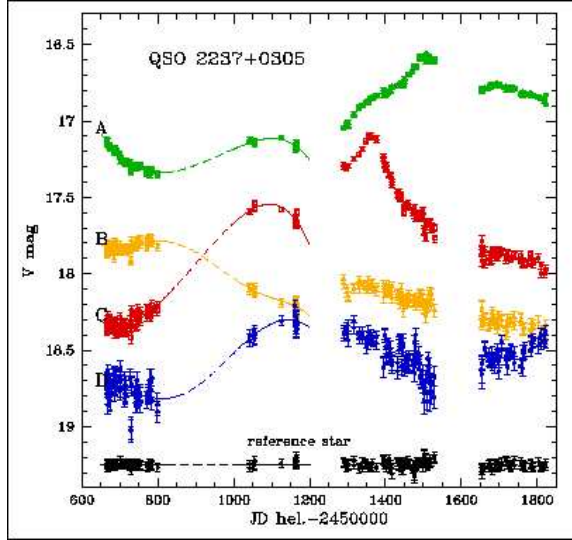


Figure 1.7: An observed light curve (visual wavelengths) for the four images of Q2237+0305, from OGLE (Optical Gravitational Lens Experiment) monitoring (Woźniak et al., 2000). Relative to the standard star, all four images of the quasar change brightness with time, over a period of a couple of years. Since the changes are not correlated between the four images, they cannot be attributed to intrinsic luminosity changes of the quasar, so are interpreted as microlensing.

$$\mu = 1/\det \begin{pmatrix} \frac{\partial x_s}{\partial x} & \frac{\partial x_s}{\partial y} \\ \frac{\partial y_s}{\partial x} & \frac{\partial y_s}{\partial y} \end{pmatrix} = 1/\det \begin{pmatrix} 1 - \frac{\partial a_x}{\partial x} & -\frac{\partial a_x}{\partial y} \\ -\frac{\partial a_y}{\partial x} & 1 - \frac{\partial a_y}{\partial y} \end{pmatrix}$$

This equation implies that, for a point source [Dirac delta function for $s(\mathbf{r}_s, t)$] at \mathbf{r}_s in the source plane, the observed brightness is $\mu(\mathbf{r}_s)$. Hence, $\mu(\mathbf{r}_s)$ is referred to as the *magnification* function, and a plot of $\mu(\mathbf{r}_s)$ over the source plane is referred to as a *magnification map*. The motion of the lensing galaxy across the line of the sight to the quasar is equivalent to the motion of the source across the magnification map. Most microlensing studies involve finding the form of the magnification map, so that light curves (brightness vs time plots) of the quasar image can be found by taking a linear cut across the magnification map (i.e. assuming that the quasar source moves across the source plane). The backward ray-tracing method for computing magnification maps is described in the next section and was utilised throughout the project.

The microlensing induced brightness variations can be distinguished from any intrinsic variation of the quasar by taking measurements of the brightnesses of all of the images of the lensed quasar. Any variations which are caused by microlensing will only occur in a single image, whereas intrinsic variations of the quasar source will be observed in all images, with a small time delay due to the different paths traversed by the rays responsible for each image. The first detection of microlensing-induced fluctuations was made by Irwin et al. (1989).

Chapter 2

Microlensing

The previous chapter gave an overview of gravitational lensing, including the basic idea behind gravitational microlensing. In this chapter, the most popular numerical method for calculating microlensing magnification maps (and the one used for the rest of the project) is described.

2.1 Backwards Ray-Shooting Method

The numerical method which was used throughout this project is the backwards ray-shooting method, similar to that developed by Kayser, Refsdal, & Stabell (1986), and extended in Wambsganss (1990)¹. Given a configuration of microlensing point masses in the lens plane, the method is able to calculate an approximate (pixellated) magnification map in the source plane. This is achieved by starting with a uniform grid of points in the lens plane. Then, for each of these points, the deflection angle is calculated by adding up the effects of each point lens in the lens plane, and the corresponding position in the source plane is calculated using Equation 1.12. Throughout the project, the code used was the code from (Wambsganss, 1990), modified so that the output files contained a list of the position of each ray in the lens plane and the corresponding position in the source plane.

For each ray, the net deflection angle is the sum of the deflection angles due to each point mass microlens. In these simulations, there were many stars, modelling a small part of the lensing galaxy, as shown in Figure 2.1 (the effect of the rest of the galaxy is taken into account by introducing external shear, see section 2.2). Thus, for each ray, the sum in Equation 1.7 consists of thousands of terms which all need to be evaluated for each ray. This is a computationally intensive process, which is sped up by the use of a hierarchical tree code (Wambsganss, 1990). In this method, for each ray, the lens plane is divided up into regions so that the deflection angle due to nearby stars is calculated exactly, but the more distant stars are amalgamated. This method was first applied to n-body simulations where the force on each particle is calculated by adding the forces due to all of the other particles (Barnes & Hut, 1986), and considerably reduces the amount of computation required as the number of stars increases (the time required is proportional to $N \log(N)$ rather than N^2 , where N is the number of stars).

When the uniform distribution of rays in the lens plane is traced into the source plane, the resulting distribution of points in the source plane is far from uniform. Areas in the source plane that collect a lot of rays correspond to areas of high magnification, and regions that don't collect many rays are places where a source at that location would not be very bright when observed through the lens. The magnification map is produced by binning the rays in the source plane, with each bin becoming one of the pixels of the magnification map. Throughout the project, the number of rays used was greater than 10^9 , ensuring that the resulting 1024×1024 pixel magnification maps were accurate and did not suffer from significant sampling error.

¹In fact, the microlensing code used during the project was a version of Wambsganss's code (Wambsganss, 1990), modified by Geraint Lewis to give positions of rays in the lens plane and the source plane.

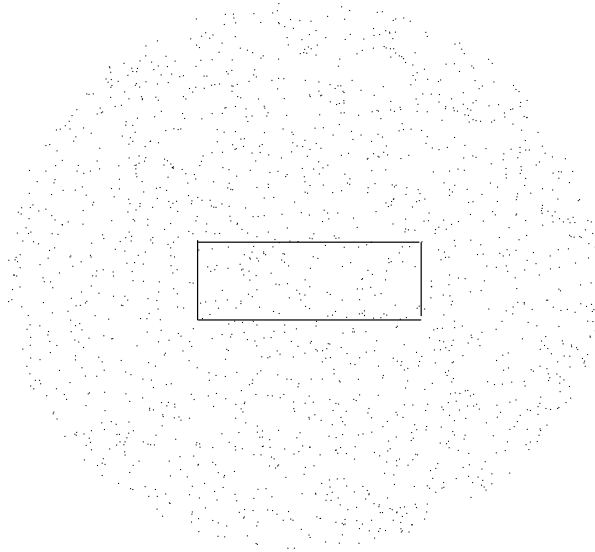


Figure 2.1: A diagram of the distribution of stars in the lens plane that was used to model a small part of the lensing galaxy. The rest of the galaxy only has an effect via the external shear parameter. The rays were fired into a uniform distribution within the rectangular region shown. Due to the external shear, this rectangular region gets mapped into a square region in the source plane, which is 20 Einstein Radii (Equation 1.8) on a side.

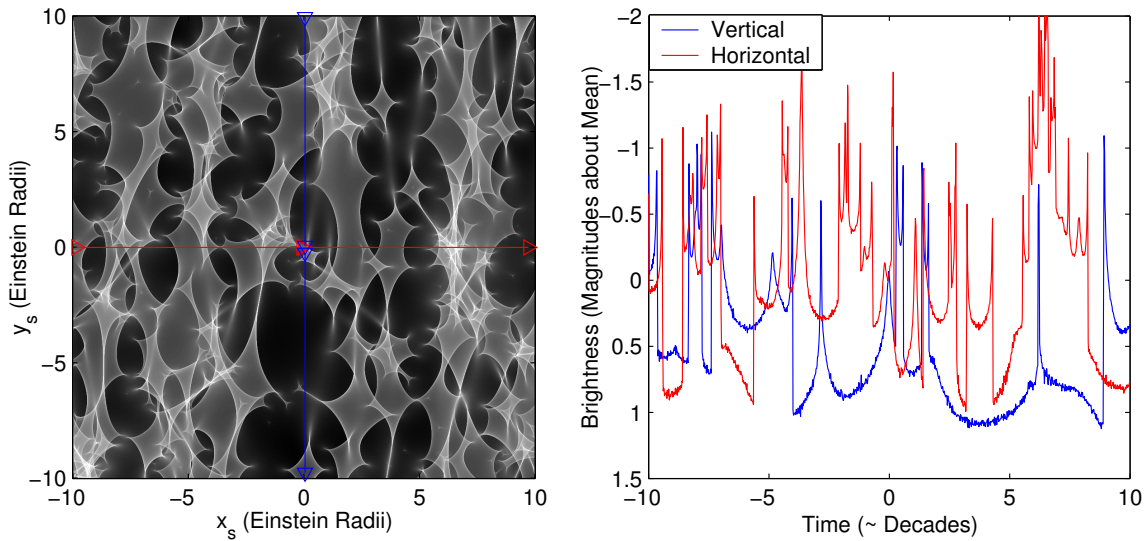


Figure 2.2: An example of a magnification map (plot of magnification vs position in the source plane) produced with the backwards ray tracing method. The white regions are high magnification whereas the dark regions are low magnification. The distance along the side of this figure is 20 Einstein Radii. On the right are light curves for a quasar taking a horizontal path or a vertical path through the middle of the magnification map (the length scale in the source plane was converted to a timescale by assuming a velocity for the quasar, see Section 2.3). The small level of noise in the light curves during the quiescent periods is due to sampling.

Figure 2.2 shows an example of a typical magnification map. The whiter regions correspond to positions where, if the quasar was there, then its image as seen through the gravitational lens would be brightened. The black areas correspond to areas where, if the quasar was there, the observed macro-image would be faint. For the most part, the range in brightnesses in the magnification map is about 2 magnitudes. The curves in the magnification map which are boundaries between bright and faint regions are caustics - that is, theoretically the magnification is infinite there (for a point source).

Plots of brightness vs time, or light curves, can be obtained by assuming that the quasar moves in some straight path across the magnification map (see Figure 2.2). In reality, this motion is mostly due to the drift of the lensing galaxy across the line of sight to the quasar. A one dimensional track across the magnification map gives rise to one possible light curve for the quasar.

2.2 External Shear

External shear is a way of incorporating the effect of the rest of the galaxy into the microlensing model, so that the individual stars that are modelled are only a small region of the lensing galaxy.

Consider a smooth matter distribution $\sigma(\mathbf{r})$ due to the entire galaxy. This produces deflection angles $a_x(x, y)$ and $a_y(x, y)$ according to equation 1.6. Let the point at the centre of the stellar field in Figure 2.1 be (x_c, y_c) . Taylor expanding the deflection angles about this point, keeping only first order terms (since the stellar region is very small compared to the scale of the whole galaxy) and writing $\Delta a_x = a_x(x_c + x, y_c + y) - a_x(x_c, y_c)$ (and similarly for Δa_y):

$$\begin{pmatrix} \Delta a_x \\ \Delta a_y \end{pmatrix} = \begin{pmatrix} \frac{\partial a_x}{\partial x} & \frac{\partial a_x}{\partial y} \\ \frac{\partial a_y}{\partial x} & \frac{\partial a_y}{\partial y} \end{pmatrix} \Big|_{(x_c, y_c)} \begin{pmatrix} x \\ y \end{pmatrix}$$

This equation gives the required modification to the deflection angles so that the effect of the rest of the galaxy can be taken into account. It can be shown (e.g. Schneider, Ehlers, & Falco, 1992) that there exists a coordinate system (found by rotating the coordinate axes) in which the matrix in the above equation takes the form

$$\begin{pmatrix} \gamma & 0 \\ 0 & -\gamma \end{pmatrix}$$

where γ is a constant called the *external shear*. In practice, to include this in the microlensing simulations, all that needs to be taken into account is that the deflection angle is the sum of that produced by the stars, and the additional external shear component

$$\mathbf{a}_{shear} = \gamma \begin{pmatrix} x \\ -y \end{pmatrix}$$

2.3 Model Parameters

Throughout the project, the microlensing parameters adopted were those appropriate to image A of the multiply imaged quasar Q2237+0305. This was the brightest image at the time of discovery, but is no longer the brightest due to microlensing-induced fluctuations (Woźniak et al., 2000). The reasons for this choice are that this particular quasar is the most well studied gravitationally lensed quasar, it is relatively bright, and since the lensing galaxy is so close ($z = 0.0394$), the timescale for microlensing is very short (decades). The redshift of

the lensing galaxy is $z = 0.0394$ and the redshift of the source is $z = 1.695$ (Huchra et al., 1985). For these redshifts, the physical size of an Einstein radius in the source plane is $D_{os}\theta_0 = 5.85 \times 10^{-2}$ pc. The effective speed of the quasar across the source plane was assumed to be $600 \frac{D_{os}}{D_{ol}}$ km s⁻¹, or approximately one Einstein radius per decade, this is simply an estimate based on the typical speed of objects in the universe relative to the Hubble flow (Kayser, Refsdal, & Stabell, 1986; Lewis & Ibata, 1998). There is an additional microlensing effect due to the individual motions of stars in the lensing galaxy, which, for a transverse velocity of 600 km s⁻¹ and a velocity dispersion of the stars of 215 km s⁻¹ (as measured for the lensing galaxy of 2237+0305) would cause a 10 per cent increase in the frequency of high magnification events (Kundic & Wambsganss, 1993). Ignoring this effect saved considerable computational effort; if the effect was taken into account then a whole new magnification map would need to be created for each point in time in order to create a light curve, increasing the computational load by orders of magnitude. The average surface mass density was taken to be $\sigma = 0.36$ (all in stars of 1 solar mass), and the external shear was $\gamma = 0.41$ (Wambsganss, Paczynski, & Katz, 1990; Schmidt, Webster, & Lewis, 1998). For this value of the surface mass density, the number of stars considered in the lens plane was 1,702.

2.4 Extended Sources

The magnification function $\mu(\mathbf{r}_s)$ gives the magnification that occurs for a point source at the position \mathbf{r}_s in the source plane. However, in reality nothing is a true point source. For the purposes of microlensing, even “point-like” quasars may have to be treated as an extended source, for which the magnification is given by equation 1.14. Note that, for an extended source with surface brightness profile $s(\mathbf{r}_s)$, centered at \mathbf{r}_c , the brightness as a function of the source centre is

$$brightness(\mathbf{r}_c) \propto \iint_S s(\mathbf{r}_s - \mathbf{r}_c) \mu(\mathbf{r}_s) d^2\mathbf{r}_s = \mu * s \quad (2.1)$$

In other words, a new magnification map for the observed brightness through the lens of an extended source, as a function of the position of the centre of the source, can be produced by convolving the magnification map for the point source with the source profile.

However, measurements have constrained the size of the UV-optical continuum source in Q2237+0305 to be $\lesssim 7.8 \times 10^{-4}$ pc in extent (Shalyapin et al., 2002). In this model, such a size translates to about a quarter of a pixel in the magnification map. This was small enough that the extended nature of the source could be ignored - effectively this makes the source the size of a single pixel.

Chapter 3

Including Cosmological Absorption

The methods described in the previous chapter can be used to calculate the magnification maps $\mu(\mathbf{r}_s)$, and hence the expected properties for the light curve of a quasar that is being microlensed by a foreground galaxy. In this study, these standard “magnification maps” still apply to the unabsorbed parts of the quasar spectrum, i.e. the continuum wavelengths, since they don’t “see” the absorption clouds. In the following sections, the method for calculating the magnification maps, and hence light curves, of the *absorbed* part of the spectrum are described. These give the flux in the Ly α absorption line as a function of the quasar’s position in the source plane, or $\mu_{absorbed}(\mathbf{r}_s)$. Together, these functions μ and $\mu_{absorbed}$ can tell us what the absorption line strength (relative to the continuum) is as a function of the quasar’s position \mathbf{r}_s in the source plane, and hence how the line strength varies with time.

3.1 Absorption Clouds

As described in Chapter 2, I made use of the microlensing code of Wambsganss (1990), modified to output the scaled positions (x, y) of the rays in the lens plane and the corresponding positions (x_s, y_s) in the source plane. The code uses the backward ray tracing method that was described in the previous chapter. In addition to the lens plane and the source plane, a third plane, the “cloud plane” was introduced, positioned between the lens plane and the source plane.

For any ray starting at a position \mathbf{r} in the source plane and landing at a position \mathbf{r}_s in the lens plane, the position \mathbf{r}_p at which that ray intersects the cloud plane is simply found by linear interpolation:

$$\mathbf{r}_p = \mathbf{r} + \lambda(\mathbf{r}_s - \mathbf{r}) \quad (3.1)$$

where λ is a parameter which determines the location of the cloud plane. If $\lambda = 0$, the cloud plane coincides with the lens plane, and can be used to model absorption clouds within the lensing galaxy (e.g. Lewis & Ibata, 2003). Alternatively, $\lambda = 1$ corresponds to the case where the absorption clouds are located at the source. This situation has been used to investigate the effects of microlensing on broad absorption line quasars (Lewis & Belle, 1998). Note that, since x, x_s , etc. are scaled distances, x_p and y_p are also scaled distances. Hence, if a point in the cloud plane has scaled coordinates (x_p, y_p) , the physical coordinates (eg. measured in parsecs) are $(X_p, Y_p) = (D_{op}\theta_0 x_p, D_{op}\theta_0 y_p)$, where D_{op} is the angular diameter distance from the observer to the cloud plane.

The structure of the clouds in the cloud plane was described by an absorption function $A(x_p, y_p)$ defined over the cloud plane, which is the fraction of photons that are absorbed as a function of where a light ray intersects the cloud plane. If a ray passes through a region where $A = 0$, it is unaffected, but if a ray passes through a region where $A = 0.5$ say, then the ray is attenuated by 50% and only counts as half a ray when the magnification map is created.

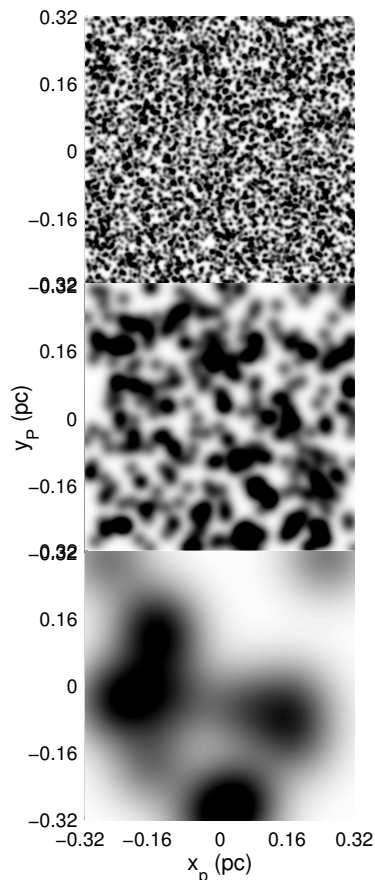


Figure 3.1: The three different absorption cloud sizes which were investigated. The cloud sizes are 0.005 pc, 0.02 pc and 0.1 pc respectively. The plots show the absorption as a function of position in the cloud plane. Black corresponds to complete absorption ($A = 1$), white corresponds to no absorption ($A = 0$). Note that due to the external shear, the rays actually pass through a rectangular area in these images (see Figure 3.3). These images of the clouds were for $\lambda = 0.2$, the physical size of the plane was different in the other two cases to ensure that all the rays passed through the cloud plane.

Since virtually nothing is known about what to expect for the small scale of structure in the Lyman Alpha clouds, a simple model for the clouds was used, with one free parameter to describe the scale of the clouds. Gaussian clouds of the form $A = \frac{1}{2}e^{-r^2/b^2}$ were generated, with clouds distributed randomly over the cloud plane, where b is a parameter called the *cloud size*. During the project, cloud sizes of 0.005 pc, 0.02 pc and 0.1 pc were investigated. The total number of clouds in the cloud plane was chosen so that the total integrated absorption over the entire cloud plane was a constant value - although this was not exact due to a clipping effect, since the absorption can never be greater than 100%. Pictures of the resulting cloud structures are shown in Figure 3.1.

3.2 Distances and Cosmology

In the model for absorption clouds, the position of the clouds between the source and the lens was described by a parameter λ , ranging from $\lambda = 0$ (cloud plane coincides with lens plane) to $\lambda = 1$ (cloud plane coincides with source plane). It is important to relate the value of this λ parameter to the redshift of the clouds, so that

if an absorption line is seen at a particular wavelength in a quasar's spectrum, the appropriate λ value for the clouds that produced that line can be identified.

The normalised lens mapping equation relating a position \mathbf{r} in the lens plane (or the image) to the corresponding position \mathbf{r}_s in the source plane is

$$\mathbf{r}_s = \mathbf{r} - \mathbf{a}(\mathbf{r}) \quad (3.2)$$

where $\mathbf{a}(\mathbf{r})$ are the scaled deflection angles in the x and y directions. Substituting for $\mathbf{r}_s - \mathbf{r}$ into Equation 3.1 gives

$$\mathbf{r}_p = \mathbf{r} - \lambda \mathbf{a}(\mathbf{r}) \quad (3.3)$$

In terms of unscaled coordinates, this reads

$$\frac{\mathbf{R}_p}{D_{op}\theta_0} = \frac{\mathbf{R}}{D_{ol}\theta_0} - \lambda \frac{D_{ls}\mathbf{A}}{D_{os}\theta_0} \quad (3.4)$$

which simplifies to

$$\mathbf{R}_p = \frac{D_{op}}{D_{ol}}\mathbf{R} - \lambda \frac{D_{op}D_{ls}}{D_{os}}\mathbf{A} \quad (3.5)$$

It is important to recognise that the derivation of equation 1.4 applies equally well if the source plane is replaced by the cloud plane. This leads to an equation similar to 1.4:

$$\mathbf{R}_p = \frac{D_{op}}{D_{ol}}\mathbf{R} - D_{lp}\mathbf{A} \quad (3.6)$$

Comparing equations 3.5 and 3.6 leads to the following important result:

$$\lambda = \frac{D_{os}D_{lp}}{D_{op}D_{ls}} \quad (3.7)$$

where D_{os} , D_{lp} , D_{op} and D_{ls} are the angular diameter distances from the observer to source plane, lens plane to cloud plane, observer to cloud plane and lens plane to source plane respectively. This equation relates the particular choice of λ to the physical location of the clouds.

For the quasar Q2237+0305, the redshifts of the source ($z_s = 1.695$) and lens ($z_l = 0.0394$) were converted to angular diameter distances using the assumed cosmology (see 1.3.1). The resulting plot of λ vs z is shown in figure 3.2. Note that the flatness of this relationship over a wide redshift range implies that the results for $\lambda = 0.95$ are approximately applicable for clouds over a very broad redshift range ($z \sim 0.5$ to $z \sim 1.695$). Hence, the very small scales of the Ly_α forest could be probed over a wide redshift range by comparing observations with the high λ simulations.

Also, the physical size X_p of any feature in the cloud plane with scaled size x_p is simply

$$X_p = D_{op}\theta_0 x_p \quad (3.8)$$

The physical size occupied by the rays that start in the rectangular region in the lens plane (Figure 2.1) and end in the square 20x20 Einstein Radius region in the source plane is plotted as a function of redshift in Figure 3.3. This determines what area of the cloud plane can have an effect on the final square in the source plane.

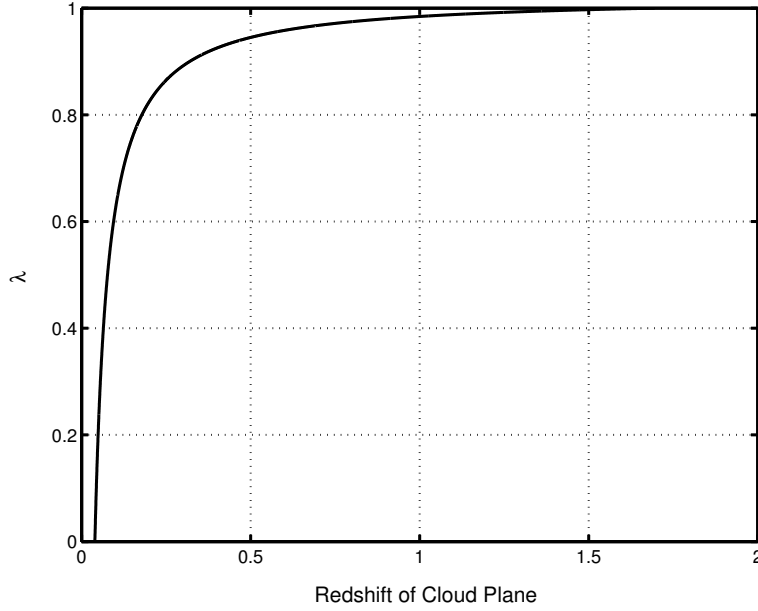


Figure 3.2: The interpolation parameter λ as a function of the redshift of the cloud plane for Q2237+0305 ($z_l = 0.0394$, $z_s = 1.695$). The relationship is highly non-linear, and shows that even for clouds at a moderate redshift of about $z = 0.5$, the corresponding λ value is close to 1.

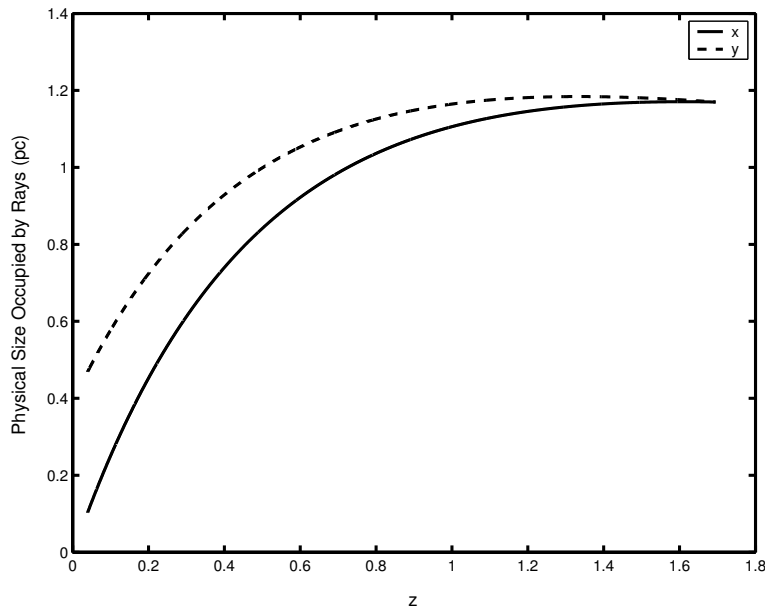


Figure 3.3: Physical size occupied by the rays which land in the main region of the source plane, as a function of redshift (between the lens and the source, $0.0394 < z < 1.695$). This relationship determines what area of the cloud plane is relevant for the rays which eventually land in the main square in the source plane. This explains why structure in the cloud plane is “blown up” in the line strength map more for clouds closer to the lens.

In this project, the cases $\lambda = 0.2$, $\lambda = 0.5$ and $\lambda = 0.95$ were investigated. For these values of λ , the corresponding redshifts for the clouds are $z = 0.049$, 0.077 and 0.53 (although, as seen in Figure 3.2, the latter result would also work well for clouds at higher redshifts). Absorption by neutral hydrogen at these redshifts would produce absorption lines in the Q2237+0305 spectrum at wavelengths of 127.5 nm, 130.9 nm and 186.0 nm respectively. While the light from the quasar may suffer significant absorption below the Lyman limit [corresponding to $z \lesssim 1$ (< 245.0 nm)] which will influence the study of the Ly_α lines, the analysis presented in this report is equally applicable to the ubiquitous metal lines that are also seen in quasar spectra and can arise at lower redshifts (Rauch et al., 2002).

3.3 Line Strength Maps

In gravitational microlensing, the magnification map $\mu(\mathbf{r}_s)$ is a function defined on the source plane, which gives what the observed intensity of the lensed image would be if the quasar source was positioned at \mathbf{r}_s in the source plane. However, in this project, I was interested in finding out how the line strength varies with time. Hence, a function $L(\mathbf{r}_s)$ was required which would describe what the line strength in the quasar's spectrum would be, if it was positioned at \mathbf{r}_s in the source plane.

In the previous section, the procedure for calculating the magnification map $\mu_{absorbed}(\mathbf{r}_s)$ for the absorbed wavelength of the spectrum was described. A measure of the line strength is the flux level at the absorbed wavelengths divided by the flux level in the neighbouring continuum region of the spectrum. This is a quantity that can be anything between 0 (deepest possible absorption line, with a flux level of zero) and 1 (weakest possible absorption line - a nonexistent one where the flux level in the "line" equals that of the continuum). This suggests the definition of a *line strength map* $L(\mathbf{r}_s)$ as

$$L(\mathbf{r}_s) = \frac{\mu_{absorbed}(\mathbf{r}_s)}{\mu(\mathbf{r}_s)} \quad (3.9)$$

This gives the strength (between 0 and 1, with 0 being the strongest) of a Ly_α absorption line in a quasar's spectrum as a function of its position in the source plane \mathbf{r}_s . As the quasar drifts across the source plane, the line strength changes. In the next chapter, line strength maps and simulated time series plots of the line strength are presented.

Chapter 4

Results

In this chapter, line strength maps are presented for the three cloud sizes (0.005 pc, 0.02 pc and 0.1 pc) and the three cloud plane positions ($\lambda = 0.2$, $\lambda = 0.5$ and $\lambda = 0.95$) that were presented in this project. Several features of them are explored, in order to determine how the properties of the line strength maps depend on the cloud size and position, and suggest ways in which the cloud sizes could be measured observationally by measuring the line strength variations.

4.1 Line Strength Maps

If the absorbing material was uniform over the small scales probed by microlensing, then the flux in the absorption line and the flux in the continuum would rise and fall together as the source moved across the source plane. In this case, the line strength map would be uniform, and a time series of measured values of the absorption line strength relative to the continuum would also be flat. Also, the distribution of magnifications [probability density function (PDF) for the magnification of a source placed at a random position in the source plane, see Wambsganss (1992); Lewis & Irwin (1995)] for the flux in the line would be the same as that for the continuum, but dimmed by a constant absorption value. Figures 4.1, 4.3 and 4.5 show line strength maps for all of the cases investigated in this project, together with magnification distributions for the continuum and the flux in the absorption line. The magnification distributions for the absorbed part of the spectrum are all essentially the same, with the most likely value having the flux in the absorption line about 1 magnitude fainter than the flux in the continuum. The discrepancies in the faint end for the larger cloud sizes are likely to be due to sampling error, with only a small number of clouds affecting the final magnification map.

For the $\lambda = 0.2$ and $\lambda = 0.5$ cases, the structure in the line strength map is complex. The caustic network from the microlensing is evident, so rapid brightness changes due to the source crossing a caustic will usually be accompanied by sudden changes in line strength, albeit not as drastic as the sudden changes in the continuum brightness. Since the rays which landed in the relevant area of the source plane occupy a smaller region of space for lower λ , only a small region of the cloud plane gets imprinted on the line strength map. Therefore, for a particular cloud size, faster variations in the line strength occur for clouds close to the source. The effect of the external shear in stretching both the magnification map and the cloud related structures in the line strength map in the vertical direction is clearly visible.

When the absorption clouds are at $\lambda = 0.95$ (close to the source), the imprint of the caustic structure becomes much less obvious in the line strength map. The line strength map in this case approximately resembles the cloud structure, so if λ is sufficiently high, the absorption can be approximated as being at the source plane, and line strength variations directly probe the structure absorbing material. As Figure 3.2 demonstrates, this approximation is applicable over a wide range of redshifts.

For the low values of λ , the rays which land in the region of interest of the source plane have only crossed a small area of the cloud plane, so the features in the line strength map are quite large. In contrast, the $\lambda = 0.95$ line strength map shows that fast variations would occur in this case.

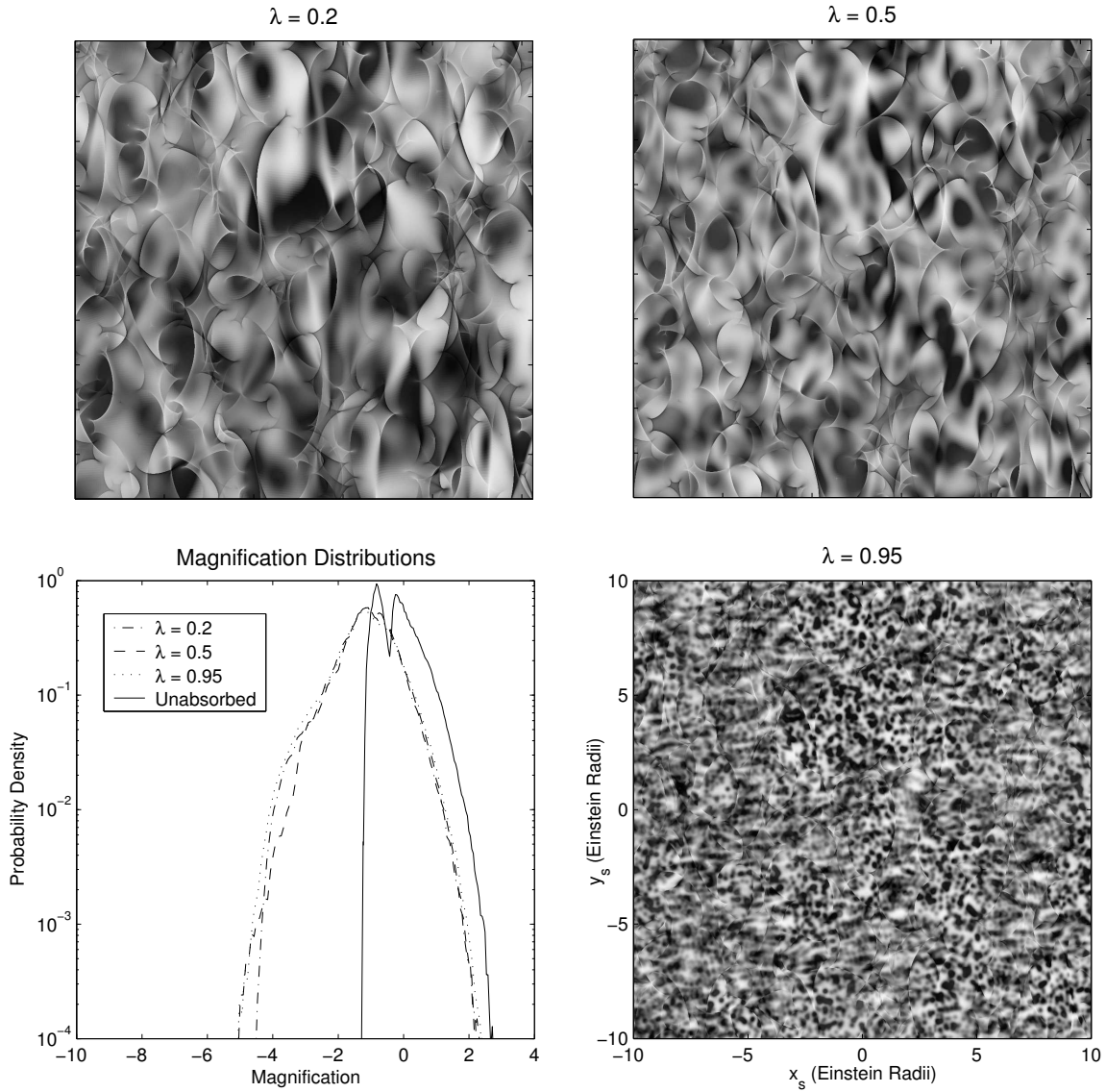


Figure 4.1: Line strength maps and magnification PDFs for the “small” cloud size 0.005 pc, for clouds at three different redshifts. Variations in the line strength occur on scales much smaller than an Einstein Radius, with the smallest structure in the line strength map (and hence faster line strength variations expected) for the clouds at $\lambda = 0.95$, close to the source. The magnification distribution shows that the continuum brightness of the quasar (unabsorbed) can vary by ~ 3 magnitudes, while the flux in the absorption line has a greater range, as it can be dimmed by the clouds.

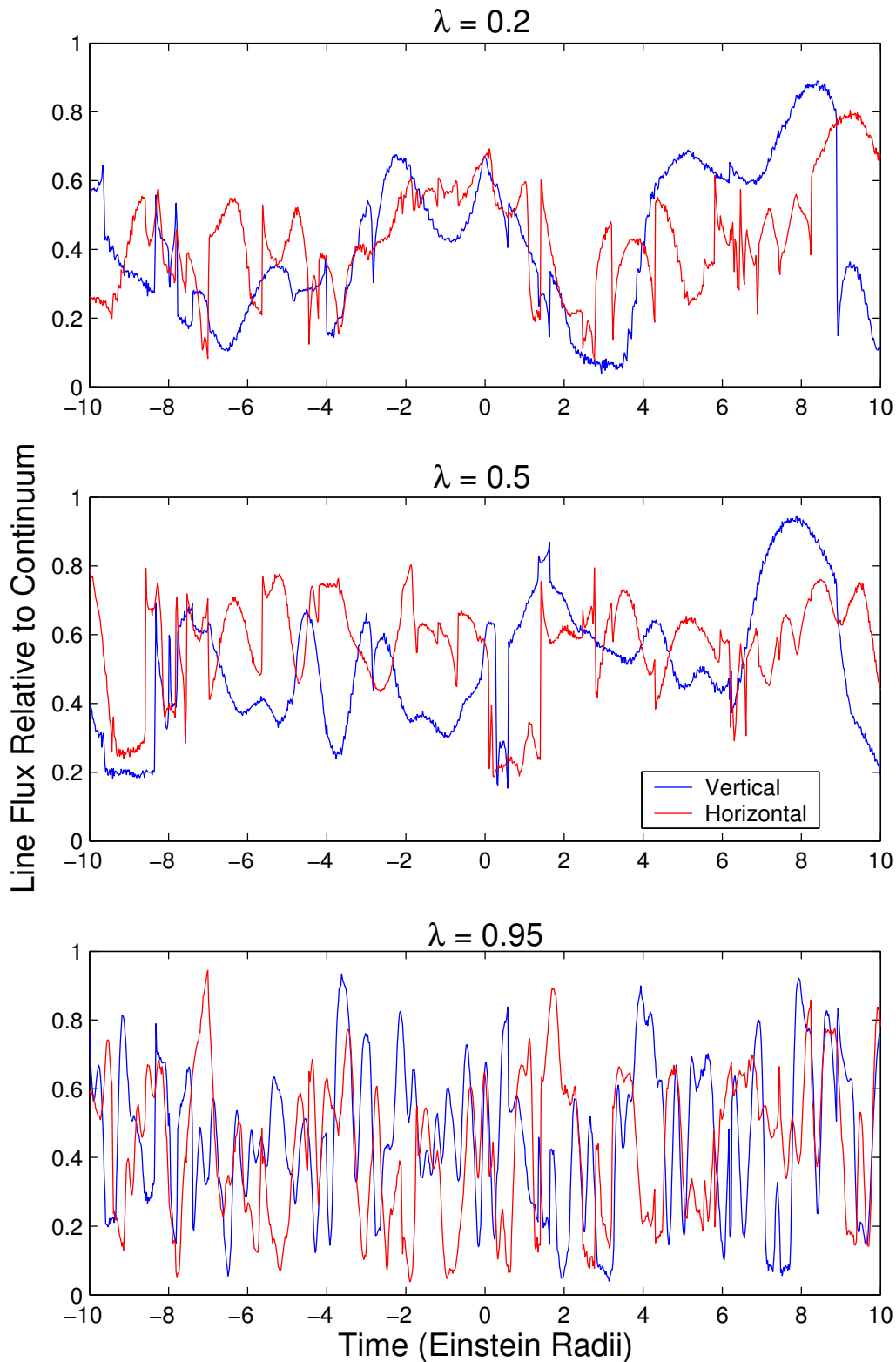


Figure 4.2: Time series of the line strengths for the small cloud case, obtained by considering a quasar that drifts along a track in the source plane through the middle of the line strength maps in Figure 4.1 (cf the tracks in Figure 2.2). Since the caustic structure is stretched out vertically by the external shear, variations are fastest for the horizontal track. For the assumed velocity of the quasar, one Einstein Radius is crossed in about 1 decade.

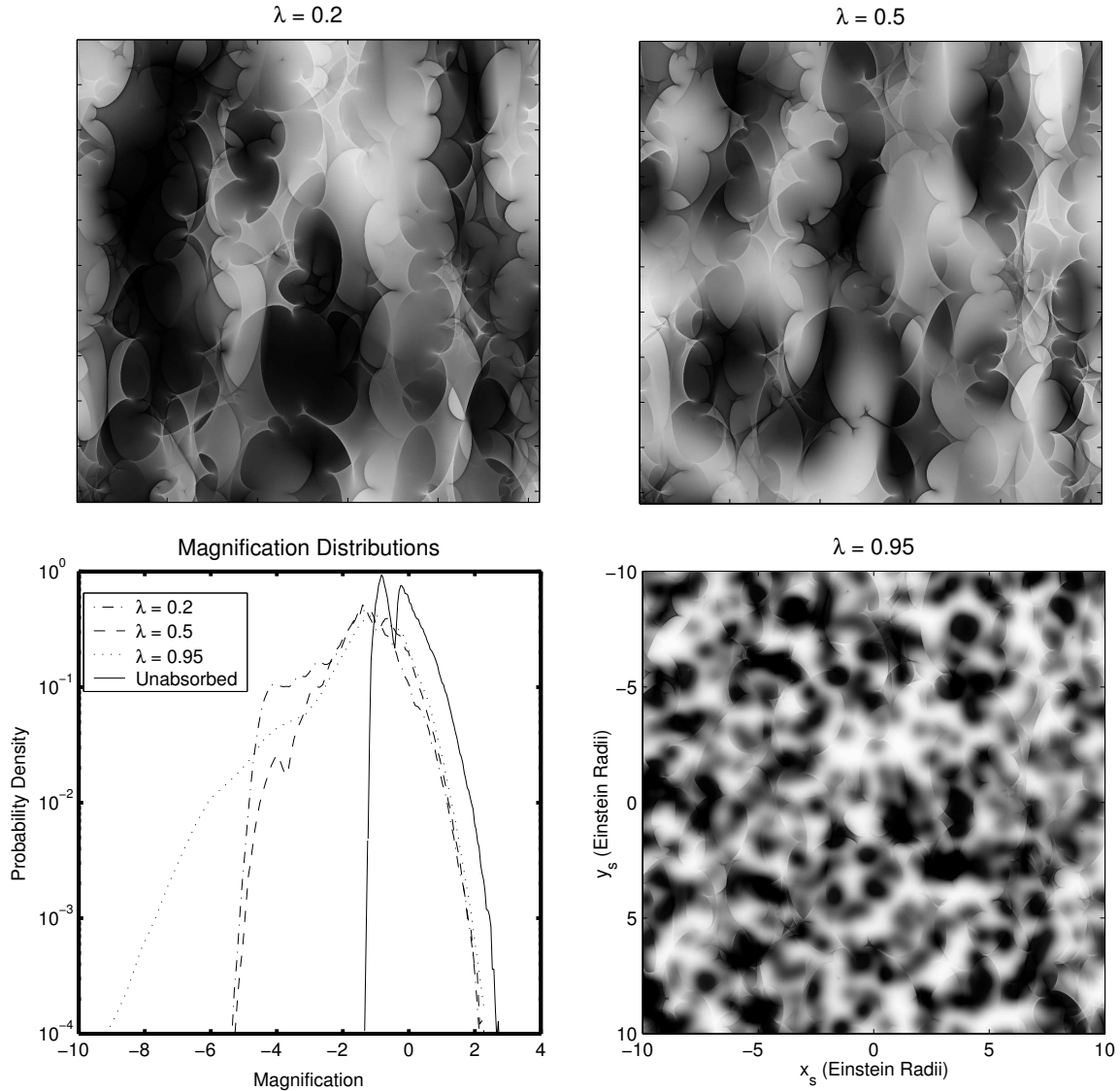


Figure 4.3: As for Figure 4.1, but for the “medium” cloud size 0.02 pc. The structure in the line strength map is on scales of about 1-3 Einstein Radii, indicating that slower variations would be expected than in the small clouds case. Once again, the caustic structure is present but is very weak in the $\lambda = 0.95$ case, which again simply resembles the cloud structure.

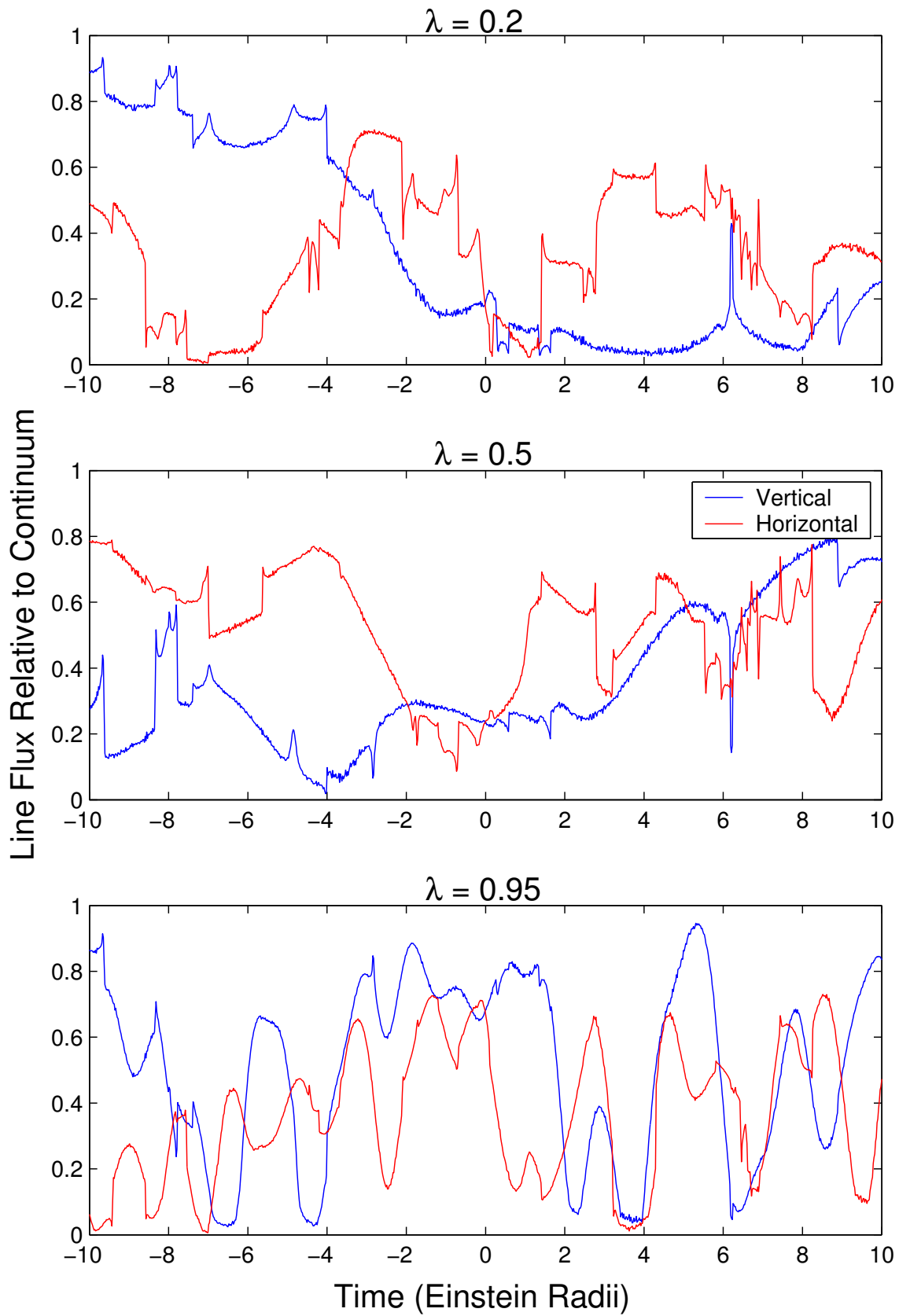


Figure 4.4: As for figure 4.2, but for the “medium” cloud size 0.02 pc. The caustic crossing events (sudden changes in line strength) can clearly be seen, except for the high λ case.

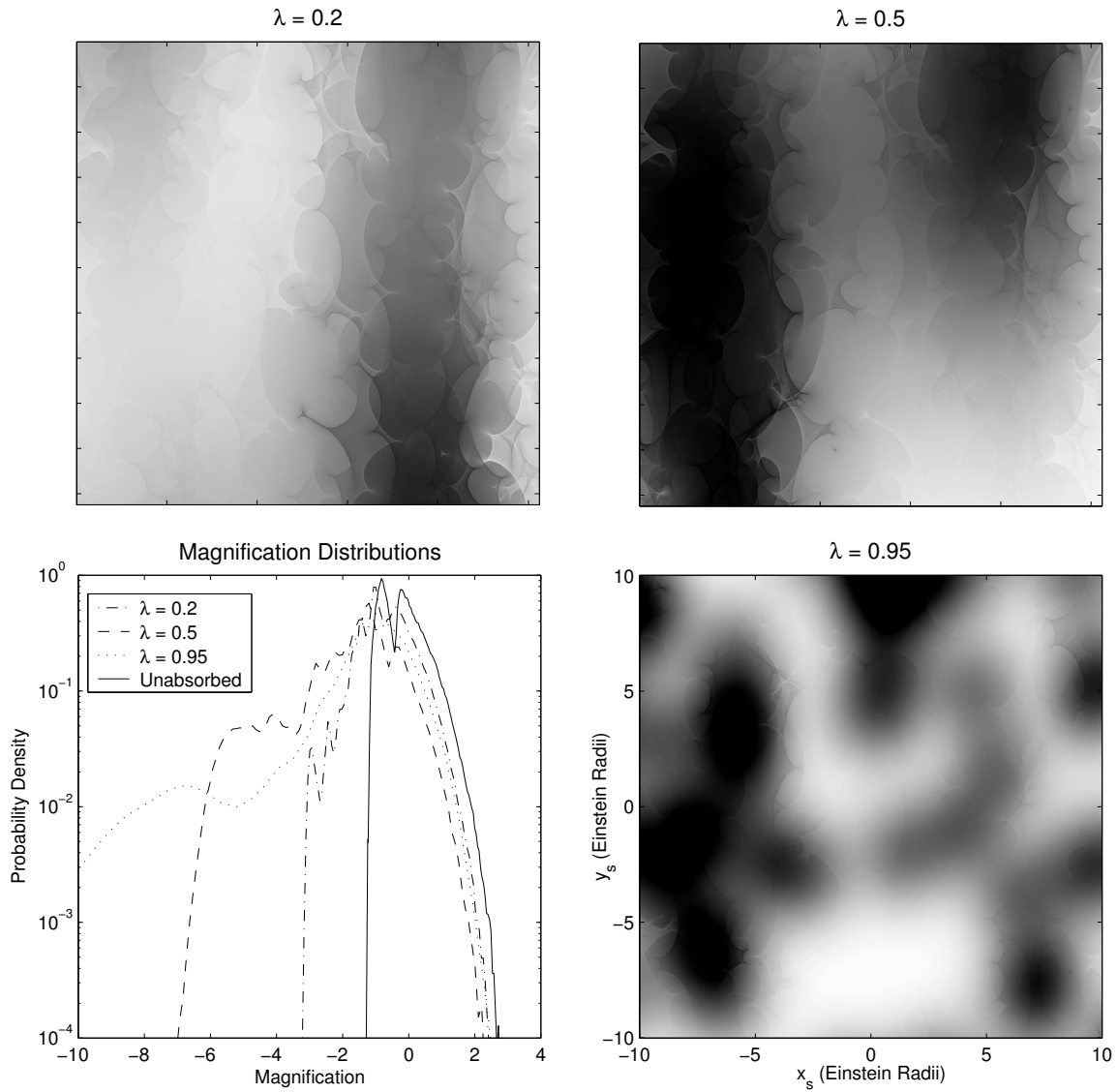


Figure 4.5: Line strength maps and magnification PDFs for the “large” cloud size 0.1 pc. Very large structures in the line strength map indicate that only very slow variations could be expected if the clouds were this large. The caustic structure is still present for $\lambda = 0.2$ and $\lambda = 0.5$, but is not as strong as for the smaller clouds.

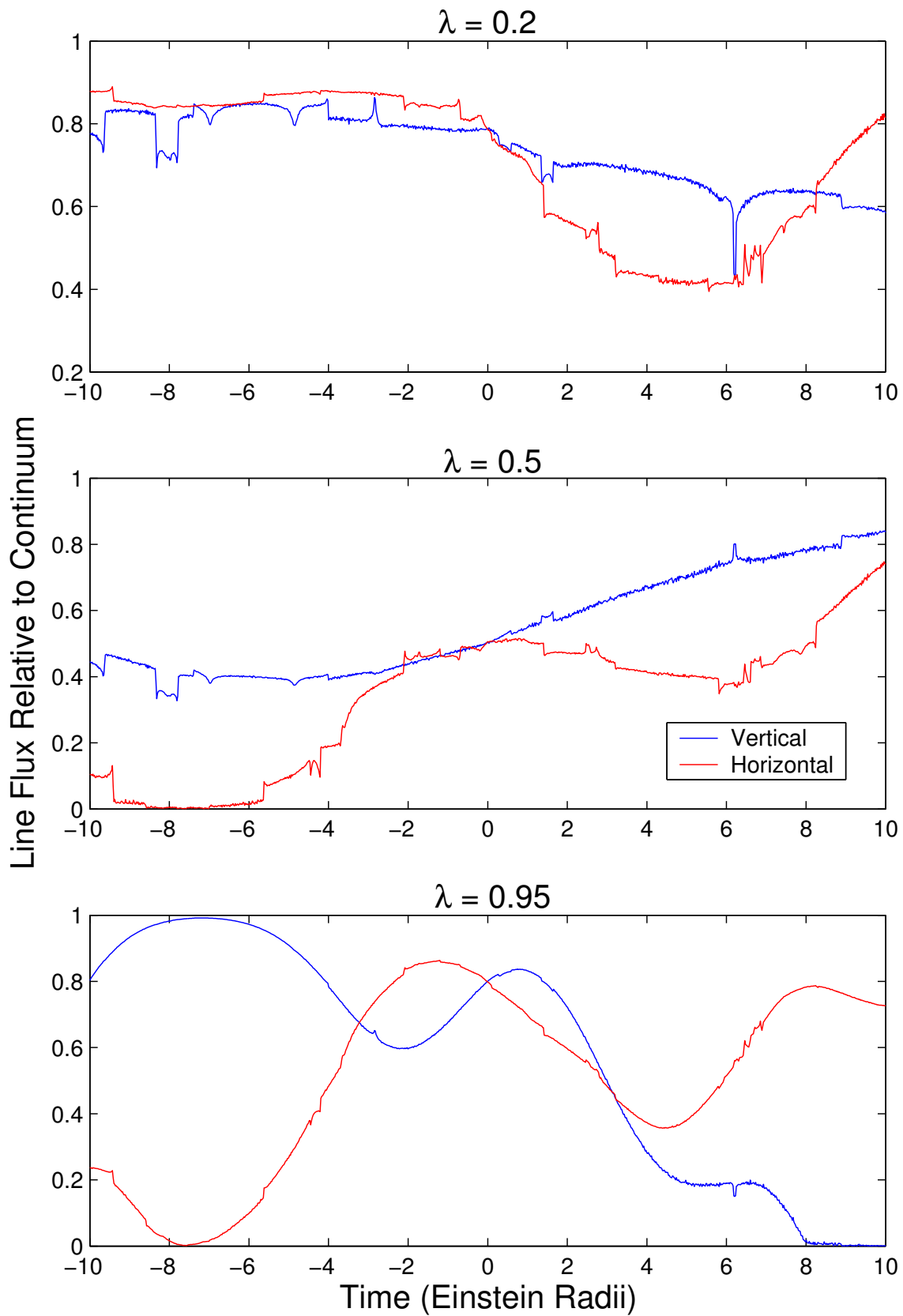


Figure 4.6: As for Figures 4.2 and 4.4, but for the “large” cloud size 0.1 pc.

Table 4.1: Time scales for line strength variation as a function of cloud size and cloud position. The units are Einstein Radii, which take approximately 9.5 years to cross.

	$\lambda = 0.2$	$\lambda = 0.5$	$\lambda = 0.95$
Small	0.33	0.24	0.09
Medium	1.14	0.81	0.37
Large	3.9	6.4	1.7

For the large 0.1 pc clouds (Figure 4.5), the line strength maps contain features that are typically several Einstein radii across, corresponding to time scales of several decades for any changes to be observed. Hence, this cloud size is approaching an upper limit of the scales that could be probed by this method. The caustic structure is still present, but the same structure is also present in the line strength maps for the other cloud sizes, so this cannot be used to distinguish different cloud sizes.

The fact that the same caustic network is present in the magnification map for the continuum and the line strength map suggests that a correlation may be present. For example, areas where the line strength would be strong may be associated with areas where the quasar has a high magnification, or vice versa. To investigate this, histograms were produced, plotting the line strength versus continuum magnification (one point for each pixel in the maps). These are shown in Figure 4.7. If there was no cloud structure so that the absorption level was constant over the cloud plane, then the flux in the line would be a constant value, so these graphs would contain a thin horizontal white line at that level, and nothing else.

An observation of a single light curve would sample regions from one of these distributions, possibly making different cloud sizes distinguishable. In each case the magnification probability distribution for the unobscured quasar source is the same. Clearly, Figure 4.7 reveals that there is no strong correlation between the continuum magnification and the line strength relative to the continuum; indeed, it does not appear to be approaching the uniform absorption case as the cloud size increases. Therefore, even though the imprint of the caustic network on the line strength maps also implies that rapid changes in the quasar brightness will be accompanied by significant changes in the line strength, there is no tendency for the changes to be correlated. Thus, the only conclusion that can be obtained from Figure 4.7 is that if any variation at all is observed, uniform absorption can be ruled out.

4.2 Time Scales

The usual way to quantify the time scale for microlensing variations is by computing the autocorrelation functions of a sample of light curves (Seitz & Schneider, 1994; Seitz, Wambsganss, & Schneider, 1994). In this case, it is the line strength variations which are being investigated, so the line strength map was used instead of the magnification map. I used a slightly different approach to measure the typical time scale for line strength variations as a function of λ and the size of the absorbing clouds. For a given line strength map, a sample of pairs of points a fixed distance apart was selected at random (see Figure 4.8), and the mean difference $\langle L_1 - L_2 \rangle$ in the line strength values between the two points was calculated.

For example, if the pairs of points are close together relative to the size of the variations, the line strength is similar for those two points, so the mean difference is small. In this way, a plot of mean difference versus separation was produced (the plots are not presented here). The separation at which the mean difference is half of its maximum value was taken to be the measure of the length scale of features in the line strength map.

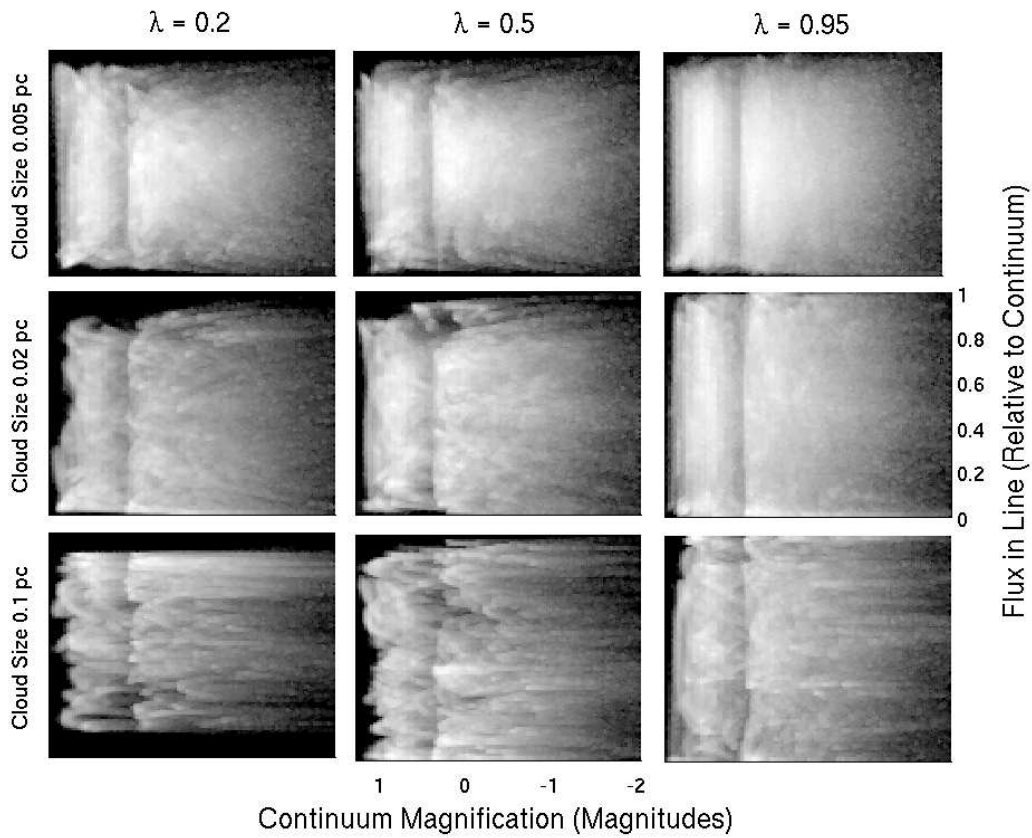


Figure 4.7: Two dimensional histograms of the line flux relative to the continuum (y axis) versus the continuum magnification (x axis) for each of the cases presented in this report. There are no strong correlations between the line strength and the continuum magnification, despite the same patterns being apparent in the maps. The dip in the magnification distribution for the continuum (Lewis & Irwin, 1995; Rauch et al., 1992) is evident in these plots.

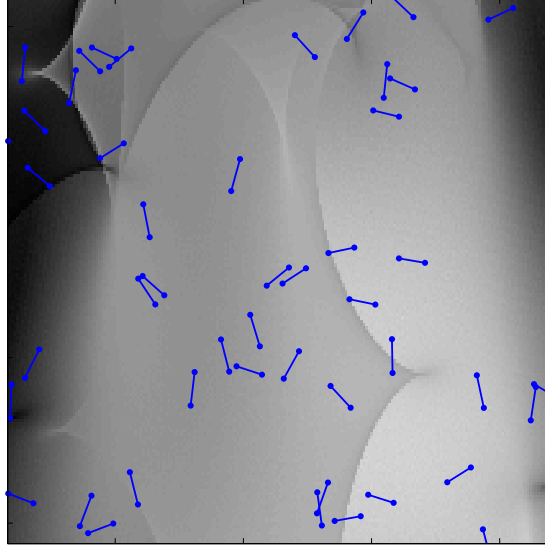


Figure 4.8: Pairs of points on the line strength map. For a given separation of the points, the mean difference in line strength can be calculated. The separation at which this mean obtains half of its maximum value defines the timescale for line strength changes.

Using the above method, the time scales for the variations for each case presented in this report were calculated (see Table 4.1). The units in the table are Einstein Radii; for the assumed transverse velocity of 600 km s^{-1} for the lensing galaxy, an Einstein Radius is crossed in about 9.5 years (see Section 3).

An examination of Table 4.1 reveals two clear trends. Firstly, as expected, variability in the line strength is most rapid for the smallest clouds. Additionally, it is apparent that the time scale of variability for a fixed physical cloud size decreases with increasing λ , and hence redshift. This implies that for a single microlensed quasar possessing identical structure throughout the Ly_α forest, the line variability will be most rapid for those absorption lines resulting from clouds closest to the quasar (remembering the non-linear relationship between λ and z presented in Figure 3.2).

The fastest variations occur for small clouds and clouds close to the source, with the variations being observable over a small number of decades for both the small and medium cloud sizes at any position between the lens and the source. The anomalous value for the largest clouds is probably due to a sampling effect, as the source plane was not large enough to be affected by many clouds.

For this effect to be measurable, there must be a significant change in the line strength over a time scale which is not too long. An absolute change of 0.25 in the line strength ought to be detectable even in low quality spectra. Recall that our measure of line strength is the ratio of the flux at the bottom of the absorption line to the flux in the nearby continuum. We measured the distribution of the waiting times for a change of 0.25 in the line strength. This was done by selecting a random starting point in the line strength map, and heading off in a random direction, moving until the line strength has changed by 0.25. The distribution of waiting times for this to occur is shown in Figure 4.9, with the corresponding medians in Table 4.2. As expected, the waiting time tends to be shortest for small clouds close to the source, and the effect is observable in a reasonable time scale for all but the largest clouds.

In an unlensed quasar, the transverse velocities of the quasar and the Ly_α clouds would also produce variations in the strength of the absorption lines. For a transverse velocity of 600 km s^{-1} , the time taken to traverse 1 pc of the cloud plane (with clouds at redshifts $z = 0.049, 0.077$ and 0.53) are 1700, 1750 and 2500 years respectively. Clearly, these are much longer than the corresponding time scales for the lensed system. For

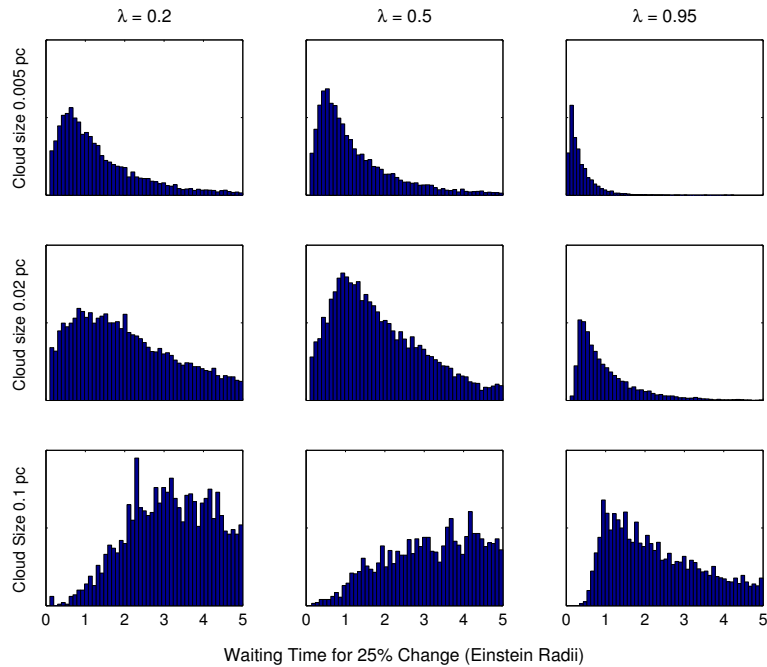


Figure 4.9: Distribution of the waiting time for a 25 per cent change in the line strength. The x-axes are all on the same scale, with the time units being Einstein Radii or about 9.5 years. The medians of these distributions are shown in Table 4.2.

Table 4.2: Medians of the waiting time distributions in Figure 4.9, in units of Einstein Radii (about 9.5 years). Note that the results for the large clouds are underestimated because the high tails of the distributions are neglected. The peak of the distributions are evident though.

	$\lambda = 0.2$	$\lambda = 0.5$	$\lambda = 0.95$
Small	0.86	0.76	0.26
Medium	1.80	1.60	0.70
Large	3.07	3.27	2.07

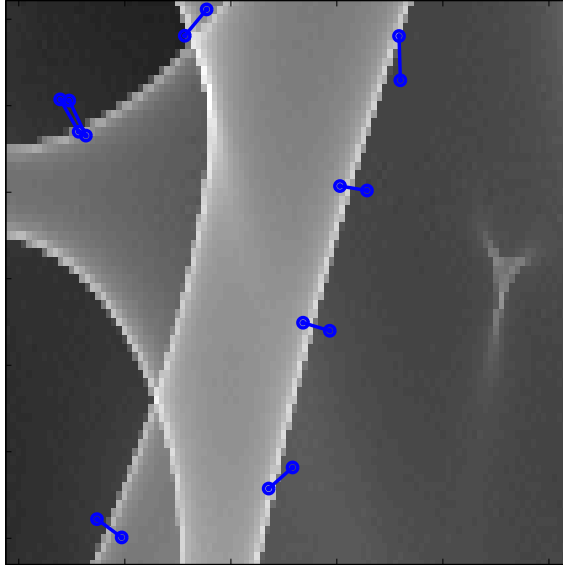


Figure 4.10: Pairs of points on the magnification map, with a magnitude difference between the two points of at least 1 magnitude. This allows a sample of caustic crossings to be investigated.

example, even for the small clouds of size ~ 0.005 pc, the time scale is $\gtrsim 8.5$ years, approximately a factor of 10 slower than the microlensed case. Thus, microlensing provides the opportunity to study the small scale structure on a reasonable time scale. For the large clouds, the effect is even more drastic. The crossing time of a cloud is ~ 2000 years, roughly 3 orders of magnitude longer than in the microlensed case.

4.3 Caustic Crossings

Since the same caustic structure from the continuum magnification map is present in the line strength maps, sudden changes in continuum brightness will be accompanied by corresponding changes in the line strength. If the absorption clouds were infinitely large (i.e. the absorption was uniform over the entire cloud plane) then there would be zero line strength changes during a caustic crossing. Therefore it is expected that, on average, the line strength change as the source crosses a caustic will be larger for the smaller clouds.

To test this possibility, the following procedure was carried out. First, a sample of points in the source plane were selected at random. For each of these points, a neighbouring point 0.05 Einstein Radii away was selected at random. This corresponds to choosing a collection of pairs of points in the source plane. If the difference in the continuum magnification between the two points of any pair was less than one magnitude, that pair of points was discarded. The list then contained pairs of points on either side of a caustic (defined by a magnitude difference in the continuum brightness between the two points being greater than 1). Then, a histogram of the corresponding line strength difference between the two points was produced. This gives the probability distribution of the line strength change, given that a caustic crossing has occurred. The histograms are shown in Figure 4.11, one histogram for each case of cloud size and λ .

The expected trend is clear - the smaller the clouds, the larger the expected line strength changes during a caustic crossing. The dependence on λ is weaker, if present at all. This result provides a way of constraining the scale of structure in the Lyman Alpha forest by taking spectra during a single caustic crossing - if the line strength does not change significantly in this time, small clouds can be ruled out.

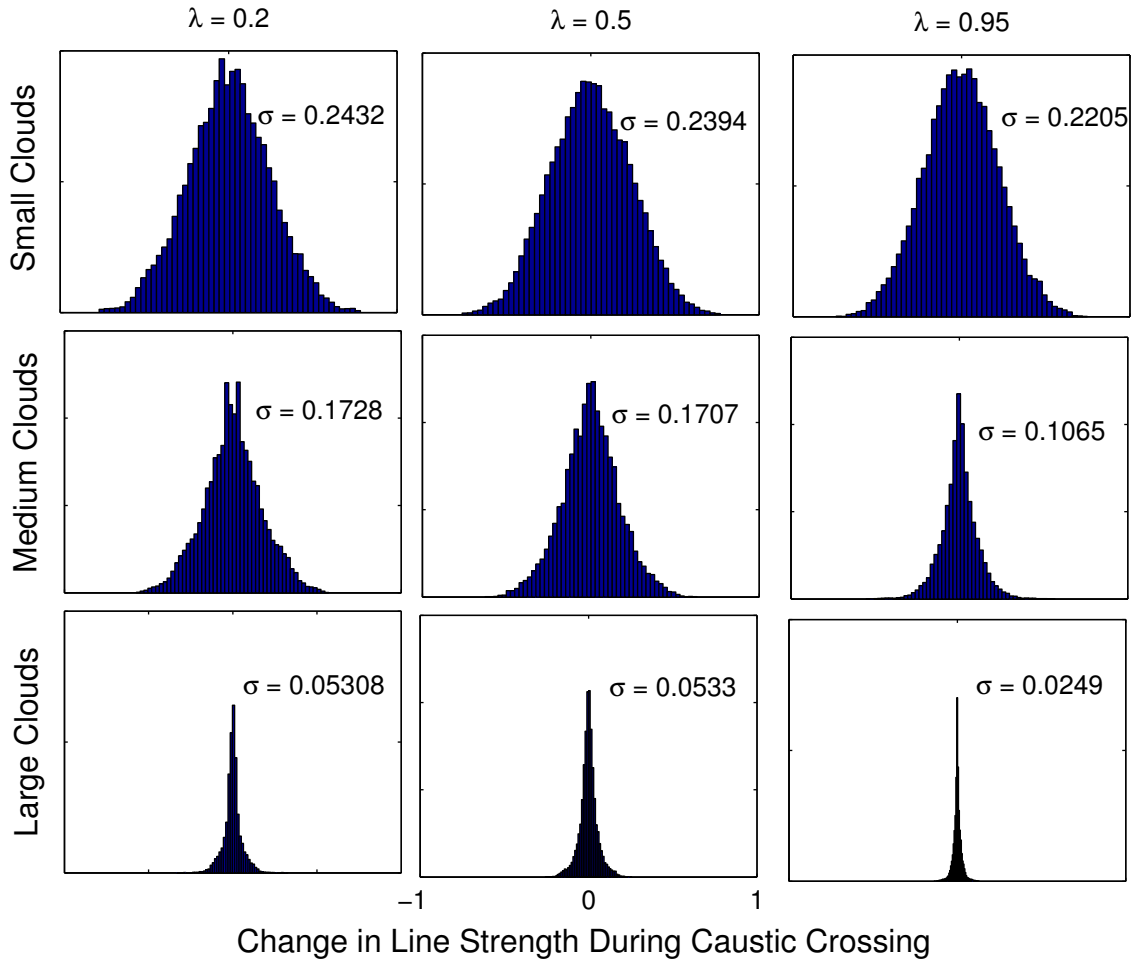


Figure 4.11: Distribution of the line strength change during a caustic crossing (defined as a greater than 1 magnitude brightness change within a 0.05 Einstein Radius interval), as a function of cloud size and position. In each case, the line strength change is approximately normally distributed. The typical sizes of the changes (given by the standard deviations σ of the distributions) is largest for small clouds. This is an expected result, because a caustic crossing corresponds to a sudden change in where the rays are travelling through in the cloud plane, and if the clouds were large then this change would not have an effect.

Chapter 5

Conclusion

The cosmological distribution of neutral hydrogen gas leaves an imprint on the spectrum of background quasars, in the form of a series of absorption lines. This phenomenon is thought to be related to the large scale flow of gas and formation of galaxies and clusters. While strong constraints have been placed on the larger scale properties of the Ly $_{\alpha}$ clouds, virtually nothing is known on smaller scales, where gas may possess similar turbulent properties to the local interstellar medium, or be collapsing to form stars. In this paper, we have examined the influence of gravitational microlensing on the paths taken by light rays impinging on a distribution of Ly $_{\alpha}$ clouds lying between the lens and the source. For a single macro-image, the population of micro-images samples differing absorption regions, with the net absorption seen (in a single line) being the average of that experienced by each ray. As the stars move, the configuration of micro-images changes, sampling different regions of the absorption clouds and causing temporal variability of the absorption line strength.

In this study I considered clouds of three different sizes and at three different locations between the lens and the source. Quantitatively, it was shown that the fastest variations in the absorption line strength occur for the smallest clouds, and for clouds close to the source. We also found that, due to the geometry of the universe, the variations in the absorption lines in the spectrum of Q2237+0305 due to clouds at redshifts $\gtrsim 0.5$ would have approximately the same effect as identical clouds which are just in front of the source. At all redshifts, the caustic structure evident in the microlensing magnification map is also present in the absorption line strength map. These discontinuities can result in very rapid changes in the absorption line strength, with a corresponding change in the continuum brightness. However, a more detailed examination of the of the relationship between the continuum magnification and the line strength shows no apparent correlation between the two.

An analysis of the variability timescales reveals that significant changes in line strength due to the effects of gravitational microlensing would be visible on time scales ranging from years to decades, dependent on the size on the size of the absorption clouds and their location behind the lens; this is at least an order of magnitude faster than clouds simply drifting across the line of sight to a distant quasar.

5.1 Further Work, Observational Prospects

Ideas for further work include:

- This study has only considered Ly $_{\alpha}$ clouds in image A of Q2237+0305, which is a positive parity image (i.e. it is not reversed). Other images of Q2237+0305 have negative parity, corresponding to one of the curves in Figure 3.3 passing through zero. Further simulations are required to fully explore the effect of image parity on the microlensing of Lyman Alpha lines.
- In this study, only absorption at a single wavelength was considered, whereas absorption clouds will possess kinematic structure which will be microlensed differently. Hence, it is possible that the detailed

shape of the absorption lines would also vary due to the action of microlensing. Also, more complicated cloud structures such as fractal structure could be investigated.

- The technique presented in this report could be used to compare the relative sizes and structure of the Lyman Alpha clouds and the associated metal line clouds, by considering the time variability of the various absorption lines, in particular, addressing the question “are the metals in the Lyman Alpha forest distributed evenly throughout the hydrogen gas?”
- In order to measure the small scale structure in the Lyman Alpha clouds, long term spectroscopic monitoring of the individual images of microlensed quasars is required. Such observations have already been proposed for studies of quasar structure (Abajas et al., 2002; Shalyapin et al., 2002; Lewis & Ibata, 2004).
- Alternatively, spectra could be taken just during caustic crossings, which can be identified by photometric monitoring such as OGLE (Woźniak et al., 2000) before they occur, and a Hubble Space Telescope override program (10123) has been waiting for several years for such an event, to obtain UV-optical spectra of Q2237+0305 during a caustic crossing event. Unfortunately, given the recent demise of STIS (Space Telescope Imaging Spectrograph), it appears the focus will have to shift to the metal lines.

Bibliography

- Abajas C., Mediavilla E., Muñoz J. A., Popović L. Č., Oscoz A., 2002, *ApJ*, 576, 640
- Barnes J., Hut P., 1986, *Nature*, 324, 446
- Becker G., Sargent W. L. W., Rauch M., 2003, *AAS*, 203,
- Brewer, B.J., Lewis G.F., 2004, *astro-ph/0410138*, accepted to *MNRAS*
- Broderick, J. 2004, Honours Thesis, School of Physics, The University of Sydney
- Davé R., Hernquist L., Katz N., Weinberg D. H., 1999, *ApJ*, 511, 521
- Ellison, S. L. 2000, Ph.D. Thesis, Institute of Astronomy, University of Cambridge
- Ellison S. L., Ibata R., Pettini M., Lewis G. F., Aracil B., Petitjean P., Srianand R., 2004, *A&A*, 414, 79
- Ellison S. L., Lewis G. F., Pettini M., Sargent W. L. W., Chaffee F. H., Foltz C. B., Rauch M., Irwin M. J., 1999, *PASP*, 111, 946
- Elmegreen B. G., 1997, *ApJ*, 477, 196
- Huchra J., Gorenstein M., Kent S., Shapiro I., Smith G., Horine E., Perley R., 1985, *AJ*, 90, 691
- Irwin M. J., Webster R. L., Hewett P. C., Corrigan R. T., Jedrzejewski R. I., 1989, *AJ*, 98, 1989
- Kayser R., Refsdal S., Stabell R., 1986, *A&A*, 166, 36
- Kayser R., Helbig P., Schramm T., 1997, *A&A*, 318, 680
- Kundic T., Wambsganss J., 1993, *ApJ*, 404, 455
- Lewis G. F., Belle K. E., 1998, *MNRAS*, 297, 69
- Lewis G. F., Ibata R. A., 2004, *MNRAS*, 348, 24
- Lewis G. F., Ibata R. A., 2003, *MNRAS*, 340, 562
- Lewis G. F., Ibata R. A., 1998, *ApJ*, 501, 478
- Lewis G. F., Irwin M. J., 1995, *MNRAS*, 276, 103
- Lewis G. F., Irwin M. J., Hewett P. C., Foltz C. B., 1998, *MNRAS*, 295, 573
- Lu L., Sargent W. L. W., Womble D. S., Takada-Hidai M., 1996, *ApJ*, 472, 509
- Marziani P., Sulentic J. W., Zamanov R., Calvani M., Della Valle M., Stirpe G., Dultzin-Hacyan D., 2003, *MSAIS*, 3, 218

Ménard, B. 2004, *astro-ph/0408276*, submitted to ApJ

McDonald P., Miralda-Escudé J., 1999, ApJ, 518, 24

McGill C., 1990, MNRAS, 242, 544

Rauch K. P., Mao S., Wambsganss J., Paczynski B., 1992, ApJ, 386, 30

Rauch M., 1998, ARA&A, 36, 267

Rauch M., Sargent W. L. W., Barlow T. A., Simcoe R. A., 2002, ApJ, 576, 45

Rauch M., Sargent W. L. W., Barlow T. A., Carswell R. F., 2001, ApJ, 562, 76

Rauch M., Sargent W. L. W., Barlow T. A., 2001, ApJ, 554, 823

Rauch M., Sargent W. L. W., Barlow T. A., 1999, ApJ, 515, 500

Rollinde E., Petitjean P., Pichon C., Colombi S., Aracil B., D’Odorico V., Haehnelt M. G., 2003, MNRAS, 341, 1279

Salpeter E. E., Hoffman G. L., 1995, ApJ, 441, 51

Sargent W. L. W., Young P. J., Boksenberg A., Tytler D., 1980, ApJS, 42, 41

Sargent W. L. W., Young P., Schneider D. P., 1982, ApJ, 256, 374

Schmidt M., 1963, Nature, 197, 1040

Schmidt R., Webster R. L., Lewis G. F., 1998, MNRAS, 295, 488

Schneider D. P., Turner E. L., Gunn J. E., Hewitt J. N., Schmidt M., Lawrence C. R., 1988, AJ, 95, 1619

Schneider P., Ehlers J., Falco E. E., 1992, “Gravitational Lensing”

Seitz C., Wambsganss J., Schneider P., 1994, A&A, 288, 19

Seitz C., Schneider P., 1994, A&A, 288, 1

Shalyapin V. N., Goicoechea L. J., Alcalde D., Mediavilla E., Muñoz J. A., Gil-Merino R., 2002, ApJ, 579, 127

Spergel D. N., et al., 2003, ApJS, 148, 175

Treyer M., Wambsganss J., 2004, A&A, 416, 19

Wambsganss J., 1990, PhD Thesis, Max-Planck-Institut für Physik und Astrophysik, München

Wambsganss J., 1992, ApJ, 386, 19

Wambsganss J., 1998, Living Reviews in Relativity, 1, 12

Wambsganss J., Paczynski B., Katz N., 1990, ApJ, 352, 407

Eric W. Weisstein. “Jacobian.” From MathWorld—A Wolfram Web Resource.
<http://mathworld.wolfram.com/Jacobian.html>

Woźniak P. R., Udalski A., Szymański M., Kubiak M., Pietrzyński G., Soszyński I., Żebruń K., 2000, ApJ, 540, L65